Universität Hamburg

Bachelor thesis in physics

Topological reconstruction of muon-decays in JUNO using the concept of Negative Photons

by

Jens Metz
born on April 15, 1993

1. reviewer: Dr. Björn Wonsak
2. reviewer: Prof. Dr. Caren Hagner

November 29, 2019

Abstract

Jiangmen Underground Neutrino Observatory (JUNO) is one upcoming experiment to observe neutrino's properties, such as their mass hierarchy. With $20\,$kton Linearalkylbenzene, 54.311 Photo Multiplier Tubes and an expected energy resolution of 3% at $1\,$MeV, it will allow to determine the hierarchy in different ways. One method will use the discrimination of electron and positron events within the detector, which show increased occurrences for one of those, depending on the mass hierarchy. Therefore, a discrimination method, constructing an artificial event of electron signature and subtracting its topological reconstruction result from an actual positron/electron event, was implemented into a topological reconstruction algorithm and applied. The remainder of this subtraction is expected to help separating positron from electron events, as an electron event would not leave any remains. The discrimination algorithm was able to annihilate an electron reconstruction result successfully and was furthermore applied on a positron event.

Zusammenfassung

Jiangmen Underground Neutrino Observatory (JUNO) ist ein neues Experiment zur Bestimmung einiger Neutrino Eigenschaften, wie z.B. deren Massenhierarchie. Mit $20\,$kton Linearalkylbenzene, 54.311 Photo Multiplier Tubes und einer vorraussichtlichen Energieauflösung von 3% bei $1\,$MeV, wird die Massenhierarchie auf mehrere Weisen messbar. Eine Methode wird die Diskriminierung von Elektronen und Positronen Events innerhalb des Detectors verwenden, da einer der Eventtypen, abhängig von der Massenhierarchie, ein erhötes Aufkommen vorweisen wird. Für diese Diskriminierung wird im Rahmen dieser Bachelorarbeit eine Verfahrensweise in einen topologischen Rekonstruktionsalgorithmus implementiert und ausgeführt, die ein künstliches Elektronen Event erzeugt und dessen topologisches Rekonstruktionsergebnis von dem eines Positronen/Elektronen Event abzieht. Die Differenz soll Aufschluss darüber geben, ob das betrachtete Event elektronenartig oder positronenartig ist. Wobei Elektronen Events keinerlei Rest aufweisen sollten. Der Algorithmus zur Diskriminierung war in der Lage, ein Elektronen Event erfolgreich zu annihilieren und wurde des weiteren auf ein Positronen Event angewandt.

Contents

1 Introduction

Neutrinos belong to the smallest and most difficultly measurable particles within the so far known types of particles. But these characteristics also provide advantages while studying our matter, earth, sun and the whole universe, since they carry information from places, where nothing else escapes as fast and as numerous as them. Such places are among others, far distant stars or the inner of our sun. To finally extract these information, one has to precisely know their behavior and properties.

Although our present Standard Model of particles did not foresee masses for neutrinos, a sophisticated physical theory was able to explain the solar neutrino problem, using a system of distinct flavour and mass eigenstates for neutrinos. The solar neutrino problem occurred during the Homestake experiment, where less electron neutrinos were measured than expected. Eventually, the idea of neutrino oscillations was able to explain the lack. This phenomena predicts, that neutrinos change their flavour, depending on travel distance, the traversed matter and the square mass difference of neutrino masses. So the absent electron neutrinos, originating from sun, just transitioned into a different flavour. This process is referred to as neutrino oscillation.

Despite the effort of constructing several neutrino experiments within the last decades, e.g. Super Kamiokande, IceCube, the exact masses of each neutrino and therefore the mass hierarchy are still subject of nowadays research. The Jiangmen Underground Neutrino Observatory (JUNO) is one of the upcoming neutrino experiments and focuses on using reactor neutrinos to solve the mass hierarchy question. In a depth of $650\,\mathrm{m}$ to the surface of a hill in China, the detector will be a sphere of $35\,\mathrm{m}$ diameter and thereby contain $20\,\mathrm{kton}$ of liquid scintillator. As soon as a charged particle crosses the liquid or emerges as a decay product, it induces light signals, which will get detected by 54.311 Photo Multiplier Tubes. A surrounding water Cherenkov detector will identify, if the signal was created by external radiation and a top tracker system will be capable of recognizing cosmic radiation, traversing the detector vertically. Two nuclear power plants, each localized in a distant of $53\,\mathrm{km}$, will serve as sources for reactor neutrinos. An outstanding feature, the detector design is expected to have a energy resolution of 3% at $1\,\mathrm{MeV}$.

Despite the focusing is set on reactor neutrinos, the energy resolution provides a perfect occasion to determine the mass hierarchy observing cosmic muon radiation. The earth's mass amplifies and suppresses certain neutrino flavour transitions of neutrinos, travelling through it, causing increased electron or positron emerging in a detector. But since the event topology of low energy electron and positron events in a liquid scintillator is similar, discriminating those becomes a challenging procedure.

This thesis introduces a discrimination method, using a concept called "negative photons", implemented into the developing Wonsak Reconstruction. The idea is to generate an artificial point-like electron event of certain energy and to subtract it from a real elec-

tron/positron event, measured in a liquid scintillator detector. The topology of the discrepancy could provide information about the original event's nature. Because a positron event consists of three spatial separated light emission sources and an electron event does not.

The second chapter of this thesis furnishes fundamental physical knowledge about neutrinos, their oscillations and sources. Chapter three focuses on the JUNO experiment, its configuration and the scintillation process. Since the discrimination method is implemented into the Wonsak Reconstruction, the reconstructions basics are elaborated within the fourth chapter. The fifth chapter explains the exact discrimination method in the way, it was included. Moreover, some reconstruction results with the applied discrimination get presented and discussed. Chapter six, summarizes the gained knowledge about the application and its functionality with suggesting prospective changes and enhancements.

2 Neutrino Physics

2.1 The Standard Model of particle physics

The Standard Model (SM) of particle physics is a conclusion of predictions by mutual gauge theories, describing the fundamental interactions such as the electromagnetic, weak and strong as fields in space and time [10]. It predicts specific fundamental particles, which get affected by these interactions or even represent such itself (see Figure 1). The only fundamental force neglected in this model is gravity, which yet can not be considered as part of it [23]. The SM contains twelve fundamental fermions, each with its own an-
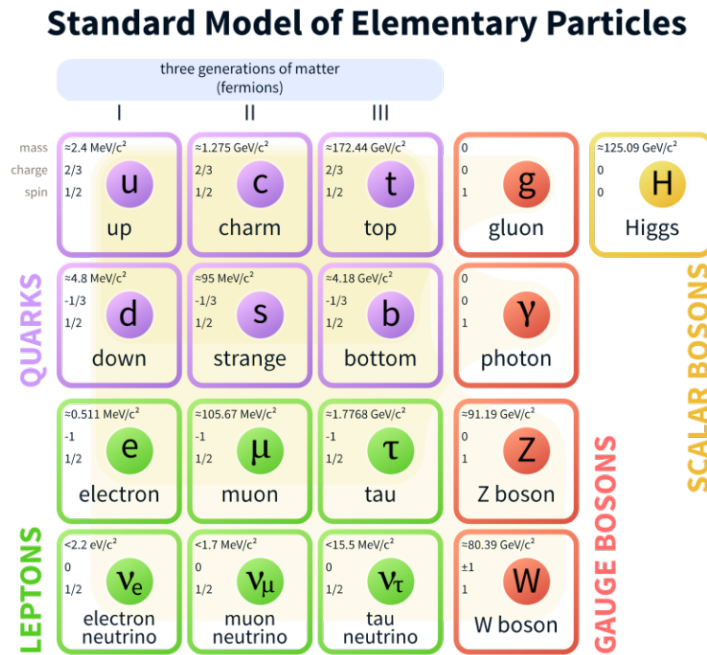

Figure 1: Standard Model particles with corresponding values for mass, charge and spin [22].

tifermion, divided into two distinct types, the Quarks and Leptons. Whereas leptons occur as individual particles, quarks only exist combined into hadrons. Since quarks carry mass, fractional electric charge and color charge, they take part in gravitational, electromagnetic and strong interactions. Furthermore they are arranged pairwise into three generations (up/down-, charm-/strange- and top-/bottom-quark).

Leptons are the electron e, muon μ, tauon τ as well as their neutrino counterparts electron-neutrino v_e, muon-neutrino v_μ and tauon-neutrino v_τ. Just like quarks, the electrons, muons and tauons carry electric charge and mass, but in contrast these leptons have electric charge of one and do not contain color charge. The neutrino's charge is zero and their masses are the very subject of nowadays scientific investigation, although the Standard Model itself does not forsee mass for a neutrino. Besides that it is still to figure out, if neutrinos are their own anti-fermions, so called Majorana fermions [29].

The last kind of particles considered by the Standard Model are the particles of the different interactions, which are bosons. Such as the photon γ, gluon g, Higgs boson H, W-boson $W^{\pm}$ and Z-boson Z, whereby the two latter represent the electroweak interaction. Particles of interactions are also referred to as force carrier or gauge bosons, which indicates their origins in non-abelian gauge theories, explicitly the quantum field theory (QFT) as an umbrella term [9]. This one combines properties of the relativity theory with the also well proven quantum theory and is based on two fundamental principles [9]. First one is that field equations – for example Lagrangians $\mathcal{L}$ [29] – must be invariant under symmetry transformations of rotation respectively translation in space as well as under time, hence gauge theories were invented. Second one is the phenomena of symmetry breaking, which occurs at reaching the lowest energy state in a system. As part of the QFT, quantum chromodynamics (QCD) describes the so called strong interaction as a non-abelian gauge theory with the gauge group $SU(3)$ and predicts eight gluons [10]. Additionally, the electroweak interaction, therefore predicted mediators are photons and $W^{\pm}$-bosons, corresponds to the $SU(2)$ gauge group, which insists on a Z-boson as one further neutral interaction particle. Hence, the product $SU(2) \times U(1)$ is used, resulting in the necessary gauge group to describe this interaction comprehensively [10]. This is where the Higgs-boson comes into account. It provides the Higgs potential, which gives masses to the $W^{\pm}$- and Z-bosons and causes the necessary symmetry break in $SU(3)$ [10]. Since one can observe parity violations in weak interactions [26], the group $SU(2)$ can get marked with an L for left-handed, meaning it just interacts with left-handed fermions. Consequently, the Standard Model ist described by the product of the non-abelian gauge groups $SU(3) \times SU(2)_L \times U(1)$ [29].

2.2 Neutrinos

At the beginning of the twentieth century, scientists could observe an energy difference between the total start and the total end energy, while examining β-decays. Thus, Pauli predicted in 1930 the existence of neutrinos and antineutrinos to explain missing momentum, angular momentum and energy. This was proven correct in 1955 by E. Reines and C.L. Cowan, demonstrated by the measurement of antineutrino caused photons in inverse β-decays. Therefore necessary antineutrinos were products of β^--decays. In their experiment an antineutrino combined with a proton leading to a new neutron and an emerging positron instead ($\bar{\nu} + p \rightarrow n + e^+$), which annihilates with a further electron emitting two gammas ($e^+ + e^- \rightarrow \gamma + \gamma$), each with an energy of $h \cdot \nu_\gamma = 0.5\,\text{eV}$ [9], with h as Planck constant and ν as the photon's frequency.

Furthermore it's been discovered, the neutrinos emerging in electron events – see the one mentioned above – can't be the same as those, which occur in events of the, in 1937 by Anderson discovered, muons. So L. Ledermann, M. Schwarz and J. Steinberger could observe in 1961. They produced rays of pions $\pi^{\pm}$, decaying into a muon μ and neutrino ν

in the two processes $\pi^+ \rightarrow \mu^+ + \nu_\mu$ and $\pi^- \rightarrow \mu^- + \overline{\nu}_\mu$ [9]. But these neutrinos ν_μ, $\overline{\nu}_\mu$ could not produce the same β-decays as observed in 1955, why it is reasonable to distinguish between ν_e, $\overline{\nu}_e$ and ν_μ, $\overline{\nu}_\mu$.

In 1975 Martin L. Perl observed the emergence of tauon-pairs $\tau^\pm$ by proving their decay products, which are muons μ^+ and electrons e^-. This decay proceeds according to $\tau^+ \rightarrow \mu^+ + \nu_\mu + \overline{\nu}_\tau$ and $\tau^- \rightarrow e^- + \overline{\nu}_e + \nu_\tau$ and leads into further kinds of neutrinos, the tauon-neutrinos ν_τ, $\overline{\nu}_\tau$, so that the lepton number L was retained and no missing energy was left [9].

Since neutrinos first got mentioned in context of β-decays and due to the importance, these processes gained for examining neutrinos, it is interesting to focus a little on this decays. Considering a given nucleon, there are three ways to induce β-decays, which retain the nucleons mass number A, but change its ordering number Z. The β^--, β^+- and electron capture [29] with the reactions:

$$(Z, A) \rightarrow (Z + 1, A) + e^- + \overline{\nu}_e \qquad\qquad (\beta^-) \qquad (1)$$

$$(Z, A) \rightarrow (Z - 1, A) + e^+ + \nu_e \qquad\qquad (\beta^+) \qquad (2)$$

$$e^- + (Z, A) \rightarrow (Z - 1, A) + \nu_e \qquad (electron \quad capture) \qquad (3)$$

or without concerning whole nucleons: Comparing the latter three equations to the reactions, introduced to explain the neutrino detection, it gets clear to see, why the decay

$$\overline{\nu}_e + p \rightarrow n + e^+ \qquad\qquad (inverse \quad \beta - decay) \qquad (4)$$

is referred to as inverse β-decay. To induce such an inverse β-decay, the anti electron neutrino $\overline{\nu}_e$ must have an energy of at least $1.8\,\text{MeV}$ [23].

2.2.1 Neutrino oscillations

When Raymond Davis in 1968 detected neutrinos originating from the sun, his team only measured about a third of the predicted neutrino flux. After the Kamiokande experiment in 1989 could confirm these result, the neutrino-, respectively flavour-oscillations became a reasonable theory to explain the lack of measurement [8].

By oscillations is meant, that a neutrino on its way from source to detector turns into a superposition of neutrino-flavours, instead of remaining one certain flavour, as they got introduced in subsection 2.1. Also new is, the neutrino-oscillation as a quantum theoretical phenomenon demands distinct neutrino masses for this case [10], which is a direct contradiction to the electroweak interaction in the Standard Model [8] but also a well known behaviour in other particle systems, e.g. quarks [29]. Eventually, the Super-Kamiokande experiment could observe significant travel distance and earth matter related behavior of neutrino flavours in 1998. This experiment detected muon and electron neutrinos, emerging from decays caused by cosmic rays in the earth's atmosphere. Some neutrinos, occurring in the atmosphere above the detector, entered the detector without a greater travel distance, whereas such, coming from the opposites earth atmosphere, had to travel a huge distance before reaching the detector. As a result, this experiment observed, the signal for electron neutrinos was not significantly different, considering the travel distances, but for muon neutrinos there was a difference. They mainly tended to oscillate into tauon neutrinos [28], which could not be detected then [10].

To understand the underlying mechanism of neutrino oscillations, the subsequent paragraph will elaborate the theoretical basement in vacuum, following the structure of sources [29] and [8].

This system interprets different flavours as distinct, orthogonal, quantum physical eigenstates $|\nu_\alpha\rangle$ (with $\alpha = e, \mu, \tau$) and treats neutrino masses the same by assigning them the orthogonal eigenstates $|\nu_i\rangle$ (with $i = 1, 2, 3$). One may notice, that there will be no necessity to limit the number of these eigenstates, as long as the total number for both types is equal. The next step is to connect the flavour eigenstates $|\nu_\alpha\rangle$ with the mass eigenstates $|\nu_i\rangle$ by introduce the unitary matrix U. It is considered for U to be real in non charge and parity (CP) violating cases [8]. This all leads us to the relations

$$\langle \nu_\alpha \,|\, \nu_\beta \rangle = \delta_{\alpha\beta} \qquad \langle \nu_i \,|\, \nu_j \rangle = \delta_{ij} \tag{5}$$

$$\mathrm{U}^\dagger \mathrm{U} = 1 \quad \sum_i U_{\alpha i} \mathrm{U}_{\beta i}^\star = \delta_{\alpha\beta} \quad \sum_i U_{\alpha i} \mathrm{U}_{\alpha j}^\star = \delta_{ij} \tag{6}$$

$$|\nu_\alpha\rangle = \sum_i U_{\alpha i} |\nu_i\rangle \quad |\nu_i\rangle = \sum_\alpha (\mathrm{U}^\dagger)_{i\alpha} |\nu_\alpha\rangle = \sum_\alpha \mathrm{U}_{i\alpha}^\star |\nu_\alpha\rangle \tag{7}$$

In antineutrino case $U_{\alpha i}$ gets substituted by $U^{\star}_{\alpha i}$, leading to

$$|\bar{\nu}_\alpha\rangle = \sum_i U^{\star}_{\alpha i} |\bar{\nu}_i\rangle \tag{8}$$

Since mass eigenstates are stationary and represent neutrinos, emitted from source $x = 0$ at time t=0, they can be expressed as

$$|\nu_i(x,t)\rangle = e^{-iE_i} |\nu_i(x,0)\rangle = e^{-iE_i t}e^{ipx} |\nu_i\rangle \tag{9}$$

where $|\nu_i\rangle$ is the initial state, E the systems energy and p the neutrino's momentum. Already at this point, it is to see, that on the very beginning of a neutrino's emerging (x=t=0), the mass Eigenstate remains the initial, which is to expect for every neutrino. Hence, the in time and space developing function for a flavour Eigenstate is just a superposition of the mass eigenstates (compare Equation 7 and Equation 9), the flavour function will inherit the above mentioned properties, just as expected. Furthermore it will become interesting to express the flavour eigenstates as superposition of all flavour eigenstates, since flavour will be the in an experiment observable property, when it causes direct measurable decays. Therefore the final flavour Eigenstate turns out to be:

$$|\nu_{flavour}(x,t)\rangle = \sum_i U_{\alpha i}e^{-iE_i t} |\nu_i\rangle = \sum_{i,\beta} U_{\alpha i}U^{\star}_{\beta i}e^{ipx}e^{-iE_i t} |\nu_\beta\rangle \tag{10}$$

The previous Equation 10 also shows the phase factor $\phi(x,t) = px - E_i t$ with the energy E_i. Using neutrinos mass m_i and momentum p_i, energy results out of the relativistic approach

$$E_i = \sqrt{m_i^2 + p_i^2} \simeq p_i + \frac{m_i^2}{2p_i} \simeq E + \frac{m_i^2}{2E} \tag{11}$$

for $p \gg m_i$ and $E \approx p$.

It ensures, due to distinct neutrino masses m_i, a unique phase factor $\phi(x,t)_i$ for each neutrino flavour. Considering the mentioned phase factor and its dependence on traveling distance as well as time, it is clearly visible how the difference in travel distance, between the observed neutrinos, affected the rate of measured muon neutrinos in the – at the beginning described – Kamiokande experiment. Also it explains, why experiments close to reactors as neutrinos sources with fixed distance, respectively travel times, are so important for observing the neutrino's behaviour.

As a next step it is interesting to take a look at the transition probability P from one flavour α to another β, for what reason the transition amplitude

$$A(\alpha \rightarrow \beta)(t) = \langle \nu_\beta \,|\, \nu(x,t)\rangle = \sum_i U^{\star}_{\beta i}U_{\alpha i}e^{ipx}e^{-iE_i t} |\nu_\beta\rangle \tag{12}$$

is to be calculated. This can be transformed into the distance dependent amplitude

$$A(\alpha \to \beta)(L) = \langle \nu_\beta \,|\, \nu(x,t) \rangle = \sum_i U^\star_{\beta i} U_{\alpha i} \exp\left(-i\frac{m_i^2}{2}\frac{L}{E}\right) \tag{13}$$

in which $L = x = ct$ marks the travel distance at the speed of light.
Eventually, the transition probability P results in

$$P(\alpha \to \beta)(t) = |A(\alpha \to \beta)(t)|^2 = \sum_i \sum_j U_{\alpha i} U^\star_{\alpha j} U^\star_{\beta i} U_{\beta j} e^{-i(E_i - E_j)t} \tag{14}$$

$$= \sum_i |U_{\alpha i} U^\star_{\beta i}|^2 + 2Re \sum_{j>i} U_{\alpha i} U^\star_{\alpha j} U^\star_{\beta i} U_{\beta j} \exp\left(-i\frac{\Delta m_{ij}^2}{2}\right)\frac{L}{E} \tag{15}$$

where Δm_{ij}^2 just describes the mass differences of two squared neutrino masses

$$\Delta m_{ij}^2 = m_i^2 - m_j^2 \tag{16}$$

.

The first addend of Equation 15 expresses the average transition probability and is both ways ($\alpha \to \beta$ or $\beta \to \alpha$) identical [29], but the second one reveals the actual spatial or time dependence of these oscillations.

As it can be derived from the previous equations for especially $A(t)$ and $P(t)$ for not CPT violating (means charge, parity and time inversion) transitions the transitions $\overline{\alpha} \to \overline{\beta}$ and $\alpha \to \beta$ would be equal. But the yet to be examined CP violation, due to the issue, that neutrinos are supposed to have a mass, would finally lead to an nonequivalent transition probability of these flavour transitions, whereas time (T) violation would lead to different probabilities in the $\alpha \to \beta$ or $\beta \to \alpha$ transitions. As mentioned, the CPT violation is still subject of nowadays research also affected by the still lasting question, if neutrinos are their own anti-particles (Majorana particle) or not (Dirac particle).

According to status quo one has to consider three flavour eigenstates $|\nu_\alpha\rangle$ – since there is ν_e, ν_μ and ν_τ –, implying three mass eigenstates $|\nu_i\rangle$. The corresponding mixing matrix U is the Maki-Nakagawa-Sakata-matrix U_{MNS}

$$U_{MNS} = \begin{pmatrix} c_{12}c_{13} & s_{12}c_{13} & s_{13}e^{-i\delta} \\ -s_{12}c_{23} - c_{12}s_{23}s_{13}e^{i\delta} & c_{12}c_{23} - s_{12}s_{23}s_{13}e^{i\delta} & s_{23}c_{13} \\ s_{12}s_{23} - c_{12}s_{23}s_{13}e^{i\delta} & -c_{12}s_{23} - s_{12}c_{23}s_{13}e^{i\delta} & c_{23}c_{13} \end{pmatrix} \tag{17}$$

with $s_{ij} = sin(\theta_{ij})$ and $c_{ij} = cos(\theta_{ij})$ (i, j = 1,2,3).

Subsequently the transition probability P for three flavours can be written as

$$P(\alpha \to \beta)(t) = |A(\alpha \to \beta)(t)|^2$$

$$= \delta_{\alpha\beta} - 4 \sum_{i>j=1}^{3} Re(U_{\alpha i}U_{\beta i}^{\star}U_{\alpha j}^{\star}U_{\beta j})sin^2\left(\frac{\Delta m_{ij}^2}{4}\frac{L}{E}\right)$$

$$+ 4 \sum_{i>j=1}^{3} Im(U_{\alpha i}U_{\beta i}^{\star}U_{\alpha j}^{\star}U_{\beta j})sin\left(\frac{\Delta m_{ij}^2}{4}\frac{L}{E}\right)cos\left(\frac{\Delta m_{ij}^2}{4}\frac{L}{E}\right)$$

(18)

In this three flavour case the probability P is sensitive to the sign of the occurring Δm_{ij}^2 as it can turn out to be negative (compare Equation 16), e.g. this influence would not exist in case of just two existing flavours [29].

Later, a more sophisticated theory got invented, also involving the influence of matter to neutrino oscillations, which will not be elaborated within this thesis as JUNO does not consider theses effects. The experiment will neglect these, since the detected reactor neutrinos just travel 53 km through the massive earth, which does not cause a significant matter effect.

2.2.2 Mass hierarchy

The first point to mention is, that the Standard Model as presented in subsection 2.1 does not foresee a mass for any neutrino. It emphasizes, particle's properties are not accurately represented by this or any comprehensive model yet.

Using the approach of neutrino oscillations (discussed in subsubsection 2.2.1), determining the neutrino's mass becomes subject of sophisticated calculations and research, since it is not an observable to measure directly. Instead the mixing angles θ_{12}, θ_{13} and θ_{23} for Equation 17 get observed and used for mass calculations.

Since Equation 18, as general theoretical approach, depends of the mass difference Δm_{ij}^2, so this is the best starting point for mass observations in vacuum oscillations yet. At least some assumptions could be established based on empirical data, namely that if there is the minimum amount of three neutrino flavours, their masses $m_{1,2,3}$ all must be unequal to each other and less than 1 eV each [21]. Since the numbering of massive neutrinos is arbitrary, the authors of the article "Neutrino Masses, Mixing, and Oscillations" in source [21] chose it in the way that $m_1 < m_2$ and identify the smallest $|\Delta m_{ij}^2|$ – by measurement of θ_{ij} calculated – with the difference of $|\Delta m_{21}^2|$ and the biggest with $|\Delta m_{31}^2|$, which is adopted to this paragraph. They furthermore explain, there are just these two independent squared mass differences $\Delta m_{21}^2 \neq 0$, $\Delta m_{31}^2 \neq 0$.

So after making the previous agreements concerning labeling, one will figure out, the possible mass hierarchies are now either $m_1 < m_2 < m_3$ (normal order) or $m_3 < m_1 < m_2$ (inverse order) [21], since it is still to figure out, if Δm_{31}^2 is positive or negative.

Current values of these mass differences Δm_{ij}^2 are (compare [21]):

$$|\Delta m_{21}^2| = (7.53 \pm 0.18) \cdot 10^{-5} \text{eV}$$

$$|\Delta m_{31}^2| = (2.51 \pm 0.05) \cdot 10^{-3} \text{eV} \quad in \quad normal \quad order$$
$$respectively$$
$$|\Delta m_{31}^2| = (2.56 \pm 0.04) \cdot 10^{-3} \text{eV} \quad in \quad inverse \quad order$$

More precisely estimated values for neutrino masses were discussed in [19]. According to it, the sum of neutrino masses $\sum_i m_{\nu_i}$ was calculated to be less than $0.23\,\text{eV}$ at a confidence level (CL) of 95% by using data of the Planck space observatory. This data joint by results of the Lyman-α forest reduces the sum to be less than $0.12\,\text{eV}$, also at 95% CL. In contrary the author also represents the outcomes of experiments in Mainz and Troitsk, constraining the electron neutrino's mass to be less than $2.3\,\text{eV}$ and $2.1\,\text{eV}$ at 95% CL, which is a direct contradiction to the in source [21] suggested assumption.

2.2.3   Reactor Neutrinos

Since the JUNO experiment mainly aims to observe neutrinos originating from reactors, it is useful to take a look on those in further detail.

Reactor neutrinos are primarily products of β^--decays [19] and therefore antielectron neutrinos $\overline{\nu}_e$. In first place neutron-rich fission daughter nucleons of ^{235}U, ^{238}U, ^{239}Pu and ^{241}Pu causes the neutrinos by β^--decays and release about six antielectron neutrinos in their whole decay channels [19], each with an energy of up to $10\,\text{MeV}$ [23] and an average of $4\,\text{MeV}$ [21]. They also emerge as result of spontaneous neutron to proton conversion after neutron capture on ^{238}U and the consequent decay of ^{239}Np [23]. A big advantage of those reactor neutrinos is that the signal channel, is the well understood inverse β-decay, but also that the detectors can be built very close to reactor sources, so that their measurement rate can get higher, compared to neutrinos of other sources [23].

In detail, the spectrum of antielectron neutrinos of a commercial nuclear power plant reactor, which consists of 58% ^{235}U, 29% ^{239}Pu, 8% ^{238}U, and 5% ^{241}Pu [23], can be seen in Figure 2, where the yield of antielectron neutrinos $\overline{\nu}_e$ per released MeV is drawn over the energy $E_{\overline{\nu}_e}$ a neutrino carries. The different colored lines represent the considered relation for ^{235}U (black), ^{238}U (red), ^{239}Pu (blue), ^{241}Pu (green) as well as the neutron capture caused process on ^{238}U (pink; consider scaling factors). The pink vertical line marks the minimum energy for inverse β-decay – as mentioned in subsection 2.2 –, so that just a third of the produced neutrinos carry enough energy $E_{\overline{\nu}_e}$ to induce inverse β-decays in detectors and every single by neutron capture created antielectron neutrino
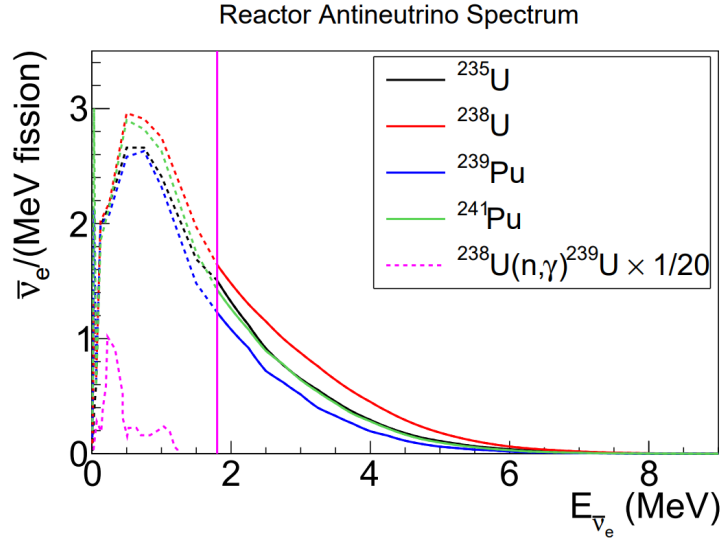
Figure 2: Amount of yielded antielectron neutrinos $\overline{\nu}_e$ per in fission released MeV drawn over the by those neutrinos carried energy $E_{\overline{\nu}_e}$. The upper lines show neutrinos from fission, whereas the lower pinkish line stands for neutron capture caused neutrinos (this one also was scaled down by the factor of 1/20 and normalized with the ^{238}U fission neutrinos for display reasons) [23].

will therefore not be observed in detectors.

2.2.4 Atmospheric Neutrinos

Although the JUNO experiment aims to observe reactor neutrinos mainly, it could turn out to be useful in future to also regard atmospheric neutrinos. Hence, it follows a short overview of these.

As atmospheric neutrinos are those referred to, which got produced by the interaction of cosmic rays and by nucleons, contained in the earth's atmosphere. Cosmic rays itself consists of about 98% hadrons – of which is 87% considered as protons, 11% as α-particles and 2% as heavier nuclei – and 2% electrons [29].

On energies E_ν up to $500\,\mathrm{TeV}$ the atmospheric muon neutrino for example stems mainly from pion and kaon decays [1], which emerge in decay chains of cosmic showers. Involved decay channels are

$$\pi^+ \to \mu^+ \nu_\mu \qquad\qquad \longrightarrow \qquad\qquad \mu^+ \to e^+ \nu_e \overline{\nu}_\mu$$
$$\pi^- \to \mu^- \overline{\nu}_\mu \qquad\qquad \longrightarrow \qquad\qquad \mu^- \to e^- \overline{\nu}_e \nu_\mu$$

$$K^\pm \to \mu^\pm \nu_\mu (\overline{\nu}_\mu)$$
$$K_L \to \pi^\pm e^\pm \nu_e (\overline{\nu}_e)$$

where the latter K decay depicts the main origin of electron neutrinos ν_e above the neutrino energy $E_\nu \approx 1\,\mathrm{GeV}$ [29,2]. In general, the amount of conventional electron neutrinos ν_e, $\overline{\nu}_e$ is less than the amount of conventional muon neutrinos ν_μ, $\overline{\nu}_\mu$. It turns out, that the ratio of both neutrino flavours $\frac{\nu_\mu}{\nu_e}$ rises up to roughly 20 reaching the energy of $1\,\mathrm{TeV}$ [2]. Conventional neutrinos mean neutrinos, produced by the above mentioned decays of pions π and kaons K. Conventional neutrinos, originated by particles, traveling horizontally through the atmosphere, turn out to have a higher energy than those, which get produced by vertically moving parent particles[1].

Another classification of atmospheric neutrinos is the prompt neutrino. They are called "prompt", since they get produced by decays of particles with especially short life times. They can be found in the sector of $1\,\mathrm{TeV}$ to $100\,\mathrm{TeV}$ neutrinos and the amount of yielded muon and electron neutrinos is equal [2]. Furthermore it is to say, the parent particles of prompt neutrinos are charmed hadrons, meaning hadrons – precisely mesons [1] – with a charm quark as heaviest component.

Both, the muon and electron neutrino, have a specific transition energy, at which the amount of conventional neutrinos gets outnumbered by the amount of produced prompt neutrinos. For muon neutrinos ν_{mu} this energy is $1\,\mathrm{PeV}$ and $30\,\mathrm{TeV}$ for electron neutrinos ν_e [2].

The appearance of tauon neutrinos ν_τ as initial atmospheric neutrinos is negligible [3].

Also it is extremely challenging to measure tauon neutrino processes at all and most of the detected atmospheric tauon neutrinos are oscillated muon to tauon neutrinos ($\nu_\mu \to \nu_\tau$) [3]. In the IceCube experiment, the probability to find such oscillated neutrinos peaks at tauon neutrinos with the energy of 25 GeV, which traveled from the opposite side of the earth's surface into the detector [3].

2.3   Spectrum of muon-decays

The experiment PINGU has its own approach to determine the mass hierarchy, using atmospheric neutrinos. Given a muon decay on the opposite side of earth, a muon neutrino ν_μ or antimuon neutrino $\overline{\nu}_\mu$ has to travel through the massive earth into the PINGU detector, where it is getting detected. Depending on the length of the travel distance and the neutrino's kinetic energy, the earth's matter affects oscillations in different significance. The $\nu_\mu \to \nu_e$ transition will be raised in case of normal mass hierarchy and $\overline{\nu}_\mu \to \overline{\nu}_e$ vice versa [24]. This results in an enhanced number of either positron or electron events within a detector. To measure increased transitions, an it is desirable, that an experiment can separate electron and positron events, which PINGU is not capable of. Still, PINGU is able to measure effects, indicating the raised transitions [32]. And although JUNO's detector volume is significantly smaller then the one of PINGU, its better energy resolution could make differences in signature of positron and electron events measurable. Thereby it may compensate for the smaller volume and consequently smaller amount of detected atmospheric neutrinos. One considered discrimination method for separating by muon decay caused electron or positron events in JUNO will be discussed in section 5.

It follows a short overview about the muon's decay channels. Processes within muon decays are described by the model of V-A interactions [6] and Table 1 provides measured muon decays with the belonging branching ratio at 90% confidence level. The branching ratio describes the amount of decays of one considered channel in a greater amount of muon decays. The ratio for the decay $\mu^- \to e^- \overline{\nu}_e \nu_\mu \gamma$ is restricted to events with a gamma energy E_γ more than 10 MeV, so one gets able to separate between this and the $\mu^- \to e^- \overline{\nu}_e \nu_\mu$ decay without photon [16].

Table 1: Measured muon decay channels expressed with negative muons although these decays with opposite charge were actually measured. 90% Confidence level [16].

Decay mode	Branching ratio
$\mu^- \to e^- \overline{\nu}_e \nu_\mu$	$\sim 100\%$
$\mu^- \to e^- \overline{\nu}_e \nu_\mu \gamma$	$1.4 \pm 0.4\%$ $(for \quad E_\gamma > 10\,MeV)$
$\mu^- \to e^- \overline{\nu}_e \nu_\mu e^+ e^-$	$(3.4 \pm 0.4) \times 10^{-5}$
$\mu^- \to e^- \nu_e \overline{\nu}_\mu$	$< 1.2\%$
$\mu^- \to e^- \gamma$	$< 1.2 \times 10^{-11}$
$\mu^- \to e^- e^- e^+$	$< 1.0 \times 10^{-12}$
$\mu^- \to e^- \gamma\gamma$	$< 7.2 \times 10^{-11}$

3 JUNO-Detector

The Jiangmen Underground Neutrino Observatory (JUNO) in China was originally planned as DAYA BAY II close to the Daya Wan nuclear powerplant and was relocated to be placed between the Yanjiang and Taishan powerplants. It is still under construction ane is expected to be finished in 2021 [25]. Once the measurements start, this experiment will observe mainly reactor neutrinos and will be able to examine supernova neutrinos, atmospheric, solar and geo-neutrinos [15].

3.1 JUNO: Physical goals

Although the main goal of JUNO is to determine the mass hierarchy of neutrinos, there are several physical goals forseen for this experiment.

Pursuing the **main goal** the experiment will look at reactor neutrinos, therefore it will measure antielectron neutrinos $\overline{\nu}_e$ originating from the two nuclear power plants, each in $53\,\mathrm{km}$ distance. They will cause inverse β-decays in the liquid scintillator (compare Equation 4), which subsequently induce a prompt and a delayed signal in the central detector [25]. Due to the positron annihilation, effectively direct after its creation, the prompt signal gets measured, whereas the delayed signal is produced by the neutron being captured by hydrogen after about $200\,\mathrm{m}s$ [25]. This signal behavior has a background, dominantly induced by the cosmogenic isotopes ^{9}Li and ^{8}He as they occur after interactions of cosmic muons traveling through the liquid scintillator [25]. There are several more – less strong – background sources, which are listed in sources [25] and [7]. The actual determination of the mass hierarchy gets conducted by measuring the energy spectrum of emerging antielectron neutrinos and the produced prompt signal, respectively, which is directly related to the survival probability of the flavour e by the effective mass squared difference (Equation 20) in Equation 19. According to [7], the probability in vacuum can be written as

$$
\begin{aligned}
P(\overline{\nu}_e \to \overline{\nu}_e) = {} & 1 - P(\overline{\nu}_e \to \overline{\nu}_\mu) - P(\overline{\nu}_e \to \overline{\nu}_\tau) - P(\overline{\nu}_\mu \to \overline{\nu}_\tau) \\
= {} & 1 - \sin^2(2 \cdot \theta_{13})[\cos^2(\theta_{12})\sin^2(\Delta_{31}) + \sin^2(\theta_{12})\sin^2(\Delta_{32})] \\
& - \cos^4(\theta_{13})\sin^2(2 \cdot \theta_{12})\sin^2(\Delta_{21}) \\
= {} & 1 - \frac{1}{2}\sin^2(\theta_{13})\left[1 - \sqrt{1 - \sin^2(2 \cdot \theta_{12})\sin^2(\Delta_{21})}\cos(2|\Delta m_{ee}^2| \pm m_\Phi^2)\right] \\
& - \cos^4(\theta_{13})\sin^2(2 \cdot \theta_{12})\sin^2(\Delta_{21})
\end{aligned}
\tag{19}
$$

with the mass squared difference shift m_Φ^2, $\Delta_{ij} \equiv \Delta m_{ij}^2 L/4E$ and $L \approx 53$, $E = E_{\overline{\nu}_e}$ and $\Delta m_{ee}^2 = \cos^2(\theta_{12}\Delta m_{31}^2) + \sin^2(\theta_{12}\Delta m_{32}^2)$ according to [7]. s_{ij} and c_{ij} represent $s_{ij} = \sin(\theta_{ij})$, $c_{ij} = \cos(\theta_{ij})$ (i, j = 1,2,3) again. The $\pm$ sign in Equation 19 stands for the corresponding mass hierarchy, $+$ for the normal hierarchy and $-$ for the inverted. Once it is clear which sign leads to the results correspondent to measurements, the mass hierarchy

can be determined. So the role the energy spectrum takes in this calculation, is that it contains the main information about the hierarchy [7] by the effective mass squared difference

$$2|\Delta m_{ee}^2| \pm \Delta m_\Phi^2 \tag{20}$$

occurring in Equation 19, with the effective mass squared difference shift $\Delta m_\Phi^2 = 4E_{vis}/L$, which depends on the distance L ($\sim 53\,\text{km}$ for JUNO) and the prompt energy E_{vis} (caused by the positrons [25] of inverse β-decay). In case of normal mass hierarchy (also look at subsubsection 2.2.2) one awaits a higher effective mass squared difference for low prompt energies (about $3\,\text{MeV}$) than for higher prompt energies (about $6\,\text{MeV}$), whereas the inverse hierarchy leads to inverse behavior [7]. Remember that for the normal hierarchy the sign in Equation 20 is chosen to be $+$ and for inverse hierarchy it is $-$. The Figure 3 shows the neutrino measuring rate (y-axes in arbitrary units) for oscillations of the normal (blue) and inverse (red) hierarchy, for oscillations of just two flavours (black) and for no oscillation (dotted), depending on the baseline L to energy E ratio (x-axis) of considered neutrinos.
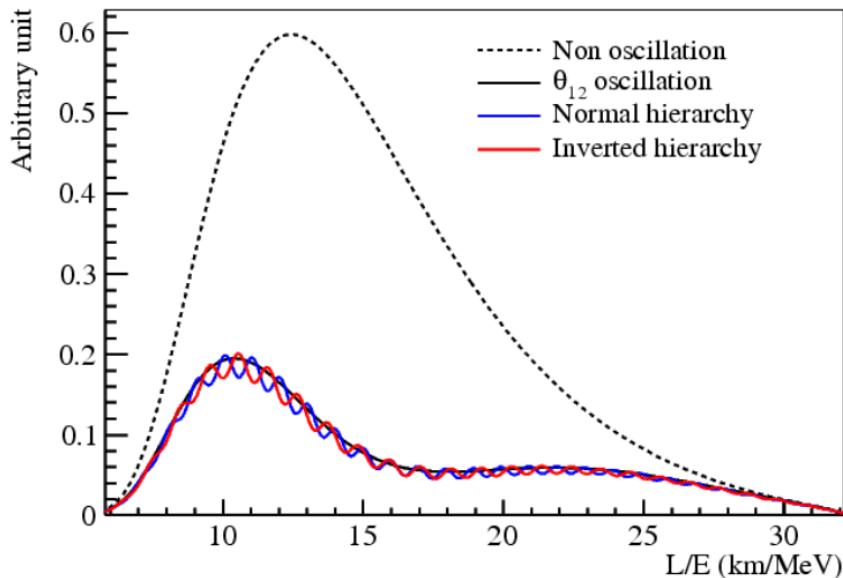

Figure 3: This graphs represent the expected neutrino measuring rate behavior (y-axis in arbitrary units) for oscillations of the normal (blue) and inverse (red) hierarchy, also for oscillations of just two flavours (black) and for no oscillation (dotted), depending on the baseline L to energy E ratio (x-axis) of considered neutrinos [7].

Furthermore, measurements of reactor neutrinos will improve the precision of the already determined oscillation parameters $\sin^2\theta_{12}$, Δm_{21}^2 and $|\Delta m_{ee}^2|$ to below 1% [18].

Another goal is to observe **solar neutrinos**. The sun is an excellent source of electron neutrinos, which might contribute to improve the understanding of, for example, the Mikheyev-Smirnov-Wolfenstein[1] effect or the solar metallicity problem, which provides

---

[1]The Mikheyev-Smirnov-Wolfenstein explains the influence of matter to neutrino oscillations.

then a better understanding of the sun [25,7]. Thanks to the low energy threshold for detected neutrinos, an energy resolution of $3\%/\sqrt{E}$, sufficient radiopurity and large mass, the JUNO detector will be well prepared to recognize those by electron scattering [25]. This scattering produces events with just one energy deposition, hence they have a huge background of natural radioactivity and cosmogenic isotopes in the detector [25].

Measuring **supernova burst neutrinos**, also by electron scattering caused by electron neutrinos and by inverse β-decay, the JUNO experiment will contribute to the research of stellar core collapses [7]. Wherefore also different detector types (gravitational-wave detectors, electromagnetic detectors, neutrino detectors) will be used as combined system [7]. Additionally the **diffuse supernova neutrino background** will get observed to gather more knowledge about the cosmic star-formation rate and the average core-collapse neutrino spectrum, but also about the rate of failed supernovae [7].

Like **atmospheric neutrinos** had an important role in prior neutrino researches, they have a significant role in nowadays researches as well. Their energies rise from 0.1 GeV to 10 TeV, distances (baselines) from detector to point of creation reach from 15 km up to 13000 km – which is troubling, since the exact creation distance is hard to estimate, but important – and these neutrinos represent every flavour [7].

Considering **geoneutrinos**, it is subject of research, to find out, how large the contribution of radioactive decays within the earth to the core's temperature is – compared to the primordial[2] heat [25]. Therefore, figuring out, the amount of U and Th in the earth by measuring antielectron neutrinos is another challenging goal for JUNO [25]. These geoneutrinos are anti neutrinos emerging as product of β-decays [7]. Which makes their recognition more challenging, taking into account, that the reactor neutrinos consist of the same type of neutrinos. But if the selection will work out, JUNO will be able to yield, with 400 events a year, the highest amount of measured geoneutrinos yet [25].

One more interesting aspect is the aspect of **sterile neutrinos**, which do not take place in actual standard weak interactions, but take part in interactions with other neutrinos [7]. Therefore, sterile neutrinos take an important role in describing anomalies in neutrino oscillations over short baselines (LSND [4], MiniBooNE [5], Reactor Neutrino anomaly [20,14], Gallium anomaly [12]) and in several sophisticated theories, like the seesaw mechanism, the leptogenesis explanation of the cosmological matter-antimatter asymmetry or they are supposedly represents of warm dark matter [17].

3.2   JUNO: The detector

The exact location of JUNO is in Jinji town, 43 km to the southwest of Kaiping city, which is a county-level city in the prefecture-level city Jiangmen in Guangdong province and has a distance of $\sim$ 53 km to the nuclear power plants in Yanjiang and Taishan. The precise distances to the different cores of these power plants are listet in Table 2 ,

---

[2]Primordial means the time in which the earth emerged.

additionally the thermal power gets listed.

Table 2: Exact distances between individual cores of the Yanjiang (YS) and Taishan (TS) power plants to the JUNO detecor as well as corresponding thermal powers [7].

Cores	YJ-C1	YJ-C2	YJ-C3	YJ-C4	YJ-C5	YJ-C6
Power (GW)	2.9	2.9	2.9	2.9	2.9	2.9
Baseline (km)	52.75	52.84	52.42	52.51	52.12	52.21
Cores	TS-C1	TS-C2	TS-C3	TS-C4		
Power (GW)	4.6	4.6	4.6	4.6		
Baseline (km)	52.76	52.63	52.32	52.20		

The actual detector will be located beneath a hill in a depth of over 650 m from the surface. The above lying earth mainly consists of granite and serves as a natural shield against cosmic rays.

A scheme of the JUNO detector is depicted in Figure 4 and can in principle be reduced into three fundamental parts. The first part is the spherical central detector, which is the main detector for most of the researches, and the second part is the water Cherenkov detector, used to suppress natural radioactivity and cosmogenic background [7,13]. A third essential part represents the muon tracker, also helping to suppress cosmogenic background. This tracker will be the top tracker from the former OPERA experiment [13].
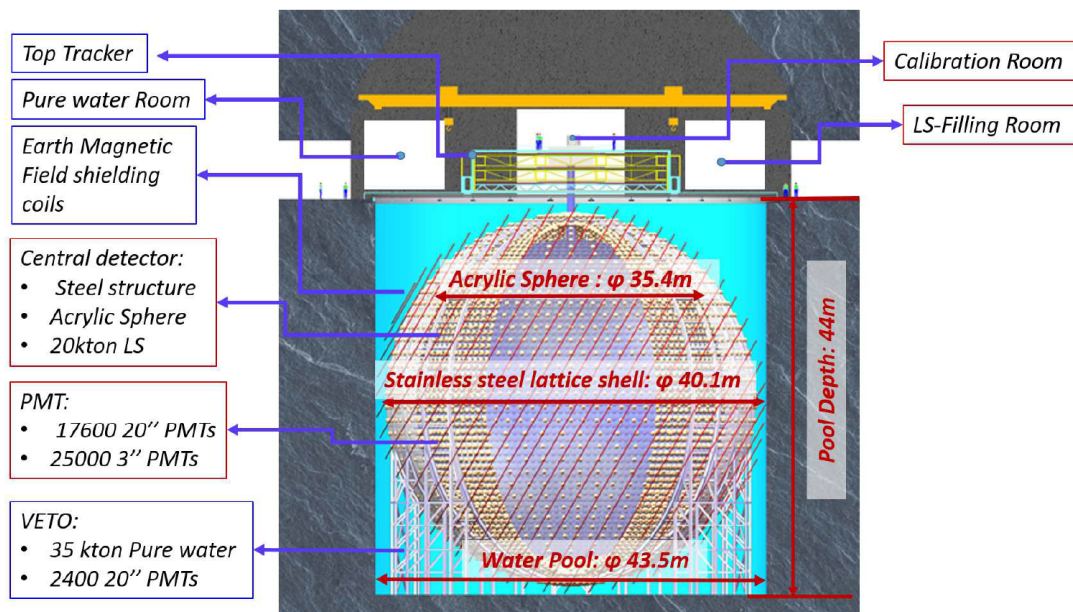

Figure 4: This is a scheme picture of the suggested detector design with the inner sphere – the central detector –, the surrounding Cherenkov detector and above deployed top tracker. All enclosed by granite in a depth of 700 m [13].

An outer stainless steel construction with the diameter of 40.1 m will support the inner acrylic sphere of 35.4 m diameter [13]. Surrounding this inner sphere, there will be

about 18000 20 inch photomultiplier tubes (PMTs) and 25000 3 inch PMTs for detecting neutrino events in the liquid scintillator [13]. These 20 kton of liquid scintillator, consisting of Linearalkylbenzene (LAB), which is transparent, with a high flash point (130 °C), low chemical reactivity and good light yield [7], will be within this acrylic sphere. Additional 2.5-diphenyloxazole (PPO) and p-bis-(o-methylstyryl)-benzene (bis-MSB) in the liquid scintillator will conduct wavelength shifting of induced photons [7] into a wavelength close to 430 nm, since the detector will aim to provide an attenuation lenght of more than 20 m at this wavelength [13]. Additionally, this wavelength provides a good quantum efficiency to get detected via PMTs. Finally the aim is to reach an overall light yield of 1200 photoelectrons/MeV.

The central detector will be placed in the cylindric pit of 43.5 m diameters, filled with ultra pure water and 2000 20 inches microchannel plate photomultiplier tubes (MCP-PMTs) on its walls. This Cherenkov detector will furthermore help to trace cosmic rays, especially muons, and also shield natural radioactivity [13]. The muon signal rate for JUNO will be ~ 3.5 Hz and the detection efficency is expected to be at 99.8% [7].

The earth magnetic field takes negative influence into the PMTs functionality, wherefore there will be field shielding coils around the big sphere [13].

On the top deployed will be the reused OPERA top tracker, covering more than 60% of the area from above and detecting about a third of the muons, which cross the central detector [13].

The detector is foreseen to measure about 10^5 events within 6 years.

3.3 Light scintillation

The JUNO detector uses scintillation light, emitted by the organic liquid scintillator Linearalkylbenzene (LAB). This emission gets caused by particles, traversing the LAB and meanwhile exciting it. To get a better understanding for this process as well as the light propagation through such a liquid scintillator, this section provides a introduction in the light scintillation.

The scintillation process can get induced by mechanical, chemical excitements, but also by radiation, interacting with a scintillator. In case of JUNO, it is the result of charged particles, exciting the molecules in a LAB and therefore losing energy according to the Bethe-equation for $-dE/dx$ [19]. The excited molecules subsequently reduce their level of excitation by emitting photons after statistical life time τ [3]. Furthermore, the wavelength spectrum of emitted photons is a material depending feature. This is why an experiment uses a liquid scintillator, providing the desired wavelength spectrum, that is optimized for the experiment's detection methods. A further ingredient to the basic scintillator is a wavelength shifter[4]. It shifts the wavelength into a spectrum, which is more transparent to the liquid scintillator, so a photon will more likely reach a photon detector and more likely get detected by it, due to the detectors wavelength sesitivity.

The luminiscence's change by travel distance dL/dx, which indicates the light yield in a liquid scintillator, is related to the energy loss of the charged particle. According to [30], its behavior corresponds to

$$
\frac{dL}{dx} = L_0 \frac{\frac{dE}{dx}}{1 + kB\frac{dE}{dx}} \quad ,
\tag{21}
$$

where kB makes a constant, individual for every material and L_0 represents the initial luminiscence. This complex behavior is caused by quenching effects and the formula was developed semi-empirical by John B. Birks [19]. The typical light yield is 3% of the excitement energy and is equal to about one photon per $100\,\text{eV}$ [30].

In order to give a description of the expected time distribution for emitted photons in a scintillator material, one has to assume, that a certain amount of excited states with a different population within an excited substance exists. Each excitement state has an individual statistical life time τ_i. Now, according to [19], the probability for an emission time to be measured is

---

[3]This time is also used to apply a first signal smearing within the descrimination algorithm in section 5, since it smears the probability density function $\Phi(\mathbf{x})$ for a real event.

[4]JUNO uses PPO and bis-MSB, providing the wavelength shift to $430\,\text{nm}$ to make sure, the photons reach an attenuation length of $20\,\text{m}$.

$$\Phi_{\mathrm{emissiontime}}(t,c) = \sum_{i=1}^{n} \frac{w_{\mathrm{i}}}{\tau_{\mathrm{i}}} e^{-\frac{t-t_0}{\tau_{\mathrm{i}}}} \quad , \tag{22}$$

with $t \geq t_0$, $\sum_{i=1}^{n} w_i = 1$ and w_{i} belonging to the individual state life time τ_{i} as a weight. Energy deposition of particles with different charges furthermore lead to different w_{i}, τ_{i}, for what reason one can recognize some particles due to their emission time spectrum in a scintillator [19].

3.4 Light attenuation

When light, i.e. photons, travel through any material, they have a chance to get attenuated. The attenuation is mainly caused by scattering and absorption effects. Relevant scatter effects are the Rayleigh-scattering on bound electrons as well as the Mie-scattering [19]. Whereas the Rayleigh-scattering explains elastic scattering at objects, much smaller than the wavelength, Mie-scattering describes scattering on objects, equal to the size of wavelength. As a photon can get absorbed, it can be reemitted in the same or different wavelength. Both, scattering and reemitting, directs a photon onto a not reconstructable way, which results into a loss of information of the event localization.
The probability function $\Phi(x, L)$, giving the likelihood of scattering or absorption, is [31]

$$\Phi(x, L) = \frac{1}{L} e^{-\frac{x}{L}} \quad , \tag{23}$$

depending on the attenuation length L and on the travel distance x of a photon. This distance is to be determined, according to

$$\frac{1}{L_S} = \frac{1}{L_{\mathrm{A}}} + \frac{1}{L_{\mathrm{are}}} + \frac{1}{L_{\mathrm{Ray}}} + \frac{1}{L_{\mathrm{Mie}}} \quad . \tag{24}$$

L_{A} represents the absorption length, L_{are} the absorption/reemission length, L_{Ray} the Rayleigh-scattering length and L_{Mie} the Mie-scattering length.

4 Wonsak Reconstruction

The Wonsak Reconstruction is a new by Björn Wonsak developed reconstruction method, which allows to reconstruct event topologies with a minimum of assumptions and without further constrains concerning the three dimensional structure of an event. The main assumption – meaning the most influencing condition – is, that the charged particle in a

liquid scintillator travels with the speed of light c_0 on a straight trajectory through the detector, whereas the second one constitutes a necessary starting condition, namely the knowledge of one certain point in time and space of the actual trajectory. This certain point is called reference point $\mathbf{r}_{ref}$ and can be provided by an independent tracking system, for example the top tracker of JUNO – as mentioned in subsection 3.2. The subsequent paragraphs will elaborate the idea of this reconstruction method, using the sources [19] and [27].

4.1 The principle

The result of this reconstruction method is information about the amount of the deposited energy, allocated to a certain three dimensional volume within a detector (referred to as event topology), using the mathematical description of a probability density function (PDF). A scheme picture of one possible outcome of a reconstruction with multiple iterations of reconstructing can be seen in Figure 5, representing a track reconstruction. Although, this thesis will subsequently consider point-like events, since the physical events, which have to be discriminated, are point-like. Further descriptions of Figure 5 follow within this section.
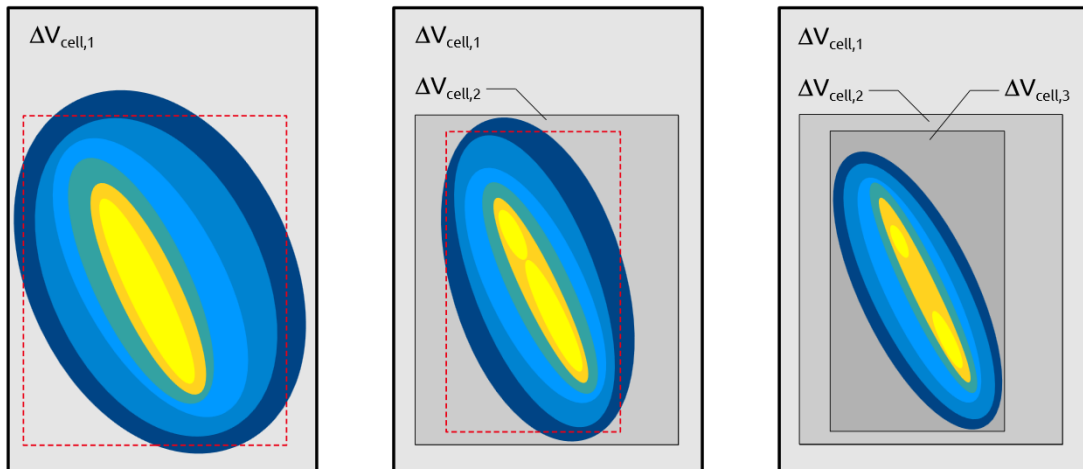

Figure 5: A scheme, showing the principle result of one, two and three iterations of reconstruction. Cold colors (blue) mark positions, that are rather unlikely part of a charged particle's trajectory. On the other hand, the warmer colors (yellow) represent more likely trajectory positions. $\Delta_{cell,i}$ names the volumina, the reconstruction method considers for a following iteration. Eventually, after each iteration, the considered volume shrinks under certain conditions until a reasonable precision in reconstructing the event is reached [19].

The principle on which the algorithm creates its estimation of the topology is best represented by the equation

$$t_j(\mathbf{x}; \mathbf{r_j}, \mathbf{r}_{\mathrm{ref}}, t_{ref}) = t_{\mathrm{ref}} \pm \frac{|\mathbf{x} - \mathbf{r}_{ref}|}{c_0} + t_{\mathrm{ph}}(\mathbf{x}, \mathbf{r_j}) - t_{\mathrm{s}} \tag{25}$$

where $t_j(\mathbf{x}; \mathbf{r_j}, \mathbf{r}_{\mathrm{ref}}, t_{ref})$ is the time at which a photon, originating from the position $\mathbf{x}$ on the trajectory, hits a PMT on position $\mathbf{r_j}$ under the assumption, the charged particle's trajectory proceeds through the reference point $\mathbf{r}_{\mathrm{ref}}$ previously or subsequently to the emission time at t_{ref}. The fact, that the reference point can be hit before or after the detection of a single photon, is addressed by using $\pm$ in the equation above. Hence, plus (+) means the reference point gets reached by the particle before the photon got emitted and vise versa the minus (-) is used.

So this detection time $t_j(\mathbf{x}; \mathbf{r_j}, \mathbf{r}_{\mathrm{ref}}, t_{ref})$ of course contains the reference time t_{ref}, but furthermore needs the particle's travel time to point $\mathbf{x}$ to be added or subtracted, considerd by the second addend.

The next one – $t_{ph}(\mathbf{x}, \mathbf{r_j})$ – adds the travel time for the detected photon, whereas t_s takes into account the further occurring several statistically (photon emission time) delays.

Since the last two addends are not to be predicted precisely, both have their own PDFs ($\Phi_{t_{ph}}(t; \mathbf{x}, \mathbf{r_j})$ and $\Phi_{t_s}(t)$) to regard all the event and system dependent factors.

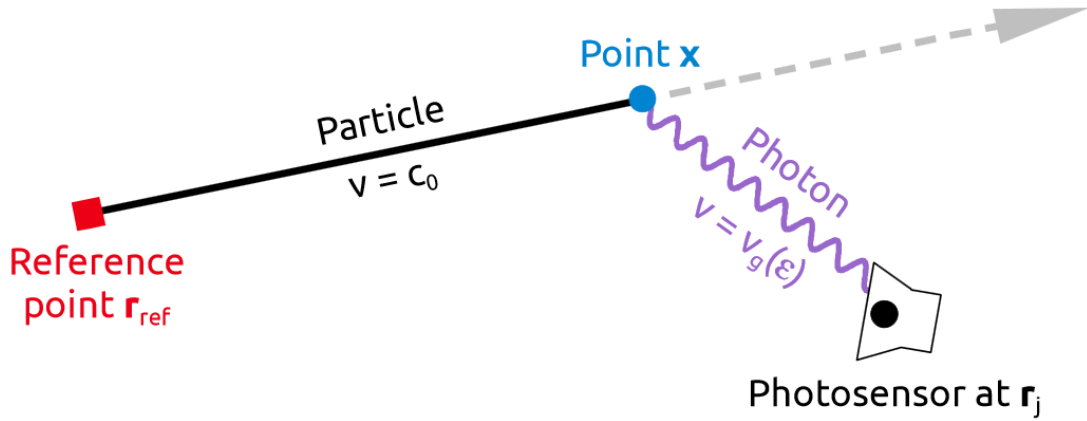Figure 6 depicts the idea of Equation 25 by showing the trajectories of the involved particles in space.

Figure 6: The charged particle passes reference point $\mathbf{r}_{\mathrm{ref}}$, reaches point $\mathbf{x}$, causes photon emission and the emerging photon gets detected by the photosensor at $\mathbf{r_j}$ [19].

A finished reconstructed event topology is a superposition of reconstruction results of each single PMT in a liquid scintillator detector. Therefore it is useful to take a look on a single PMT's proceedings first. The reconstruction algorithm will dedicate an number of points $\mathbf{x}$ as possible origins – for a detected photon – to a PMT as the algorithm solves Equation 25 for x. Figure 7 shows a PMT position, a reference point position and several black lines (also referred to as isochrones). Each black line represents the number of $\mathbf{x}$, that would lead to the one detection time $t_j(\mathbf{x}; \mathbf{r_j}, \mathbf{r}_{\mathrm{ref}}, t_{ref})$ for given $t_{ph}(\mathbf{x}, \mathbf{r_j})$ and t_s.

This means, every detection time gets distributed its own black line.

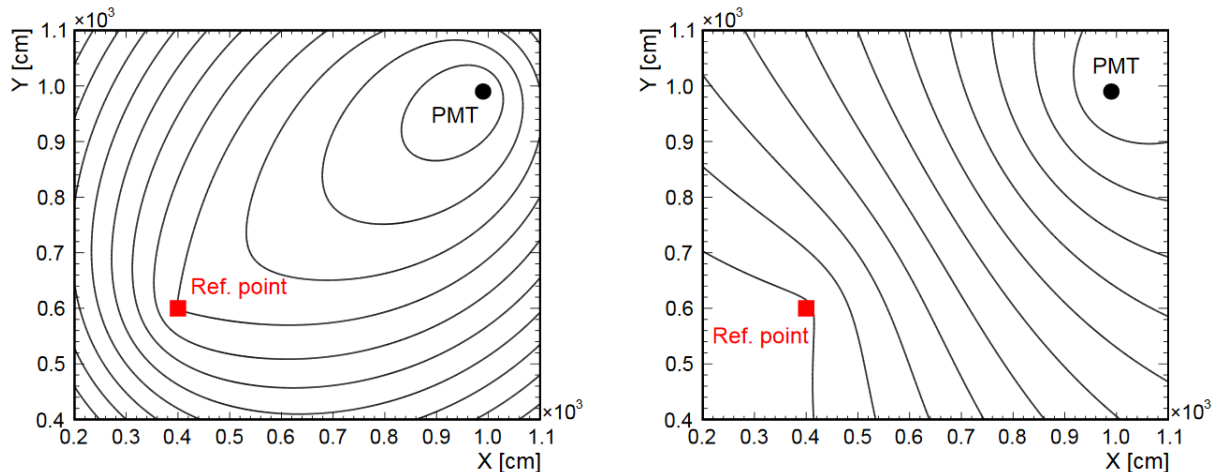Figure 7: Single PMT's reconstruction results for possible photon origin **x** under assumption of photon emission after the charged particle proceeded through reference point (left panel) and before (right panel). Each black line represents the positions **x**, leading to the exact same detection time $t_j(\mathbf{x}; \mathbf{r_j}, \mathbf{r_{ref}}, t_{ref})$ [19].

The left panel in Figure 7 was created with the assumption, that the charged particle first reaches the reference point and subsequently caused the detected photon, on the other hand the right panel was created with the opposite assumption. As the actual reconstruction topology is three dimensional, one can imagine the actual result as these panels, spinning around an axis between reference point and PMT position. Taking the statistical uncertainty about photon emission, this ends up in getting reconstruction results like the left picture in Figure 8, where not distinct lines but colored areas mark isochrones, with the warmer colors (yellow) indicating most likely original emission points. The left panel also shows the dominant influence of the time distribution function Φ_{t_s}, which gets a little more elaborated in subsubsection 4.1.1. On the other hand, the right panel shows the result after considering a spatial detection efficiency $\epsilon_j(\mathbf{x})$.

Due to the probability dependencies mentioned above, the equation Equation 25, that is to solve for each detected photon k and each PMT j, results into the PDF

$$\Phi_{j,k}(\mathbf{x}) = w_{j,k}\epsilon_j(\mathbf{x}) \int_0^\infty \Phi_{t_s}(\Delta t)\Phi_{t_{ph}}(t'; \mathbf{x}, \mathbf{r_j})dt' \tag{26}$$

with $w_{j,k}$ as normalization factor, the spatial detection efficiency $\epsilon_j(\mathbf{x})$ as well as the both prior invented PDFs $\Phi_{t_{ph}}(t; \mathbf{x}, \mathbf{r_j})$ and $\Phi_{t_s}(t)$.

The Δt stands for $\Delta t = t_{j,k} - t_j(\mathbf{x}; t_{ph} = t', t_s = 0)$ in which $t_{j,k}$ is the expected hit time for this photon k and PMT j. t' is the measured hit time.
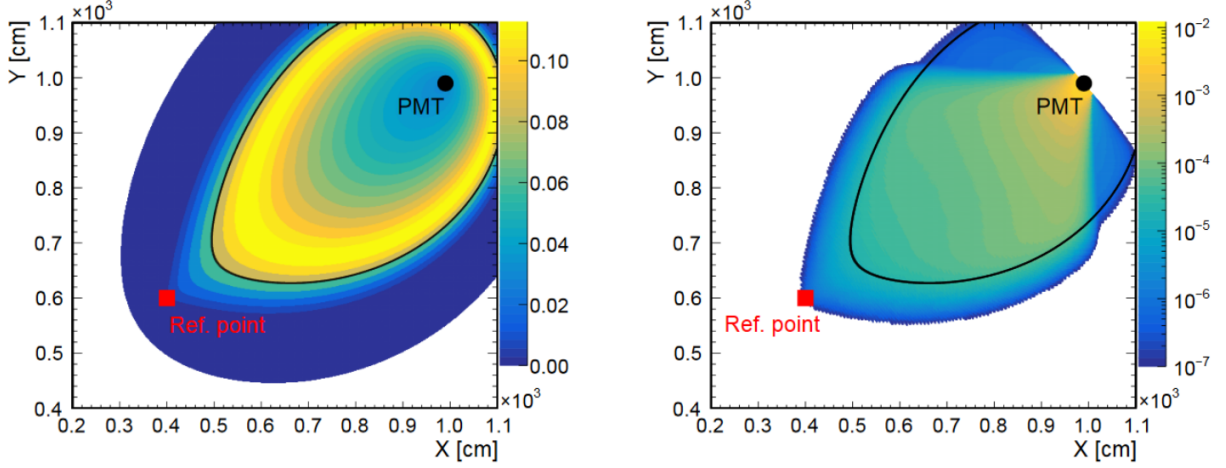
The normalization factor $w_{j,k}$ gets defined by

Figure 8: Single PMT's reconstruction results for possible photon origin **x**. Left panel shows a detecting PMT without physical constraints and the right one shows the result, taking into account the spatial detection efficiency $\epsilon_j(\mathbf{x})$. Each colored area represents possible positions **x**, where equal colored areas lead to the exact same detection time $t_j(\mathbf{x}; \mathbf{r_j}, \mathbf{r_{ref}}, t_{ref})$ and warmer colors (yellow) indicate more likely isochrones [19].

$$w_{j,k}^{-1} = \int_{V_{LS}} \epsilon_j(x) \int_0^\infty \Phi_{t_s}(\Delta t) \Phi_{t_{ph}}(t'; \mathbf{x}, \mathbf{r_j}) dt' dV \qquad (27)$$

so that it fulfills the condition

$$\int_{V_{LS}} \Phi_{j,k}(\mathbf{x}) dV = 1 \quad . \qquad (28)$$

To obtain the PDF for all detected photons and PMTs it is necessary to sum all the $\Phi_{j,k}(\mathbf{x})$ according to

$$\Gamma_{det}(\mathbf{x}) = \sum_{j,k} \Phi_{j,k}(\mathbf{x}) \quad . \qquad (29)$$

Additionally, by rescaling $\Gamma_{det,j}(\mathbf{x})$ using the global detection efficiency $\epsilon(\mathbf{x})$, it is possible to get the spatial density distribution of even all emitted photons:

$$\Gamma_{em}(\mathbf{x}) = \frac{\Gamma_{det}(\mathbf{x})}{\epsilon(\mathbf{x})} \quad . \qquad (30)$$

With the global detection efficiency just being the sum of all individual detection efficiencies from Equation 26.

It is to mention, that estimating the whole deposited energy in an event is limited. So if a detector is not able to measure all created photons, but can detect the first caused

photons, the algorithm cannot provide energy information, but it would still be capable of reconstructing the event topology in space and time.

4.1.1 Time distribution function

Since the time distribution function Φ_{t_s} will have an emphasized role for positron, electron discrimination, it appears to be important to elaborate this.

Among other things, this function assigns a certain probability to a specific emission time of a single photon after the excitement of molecules in a liquid scintillator. This means, a photon possibly does not get emitted directly after a charged particle exited emission to molecules. It is more likely, that emission starts very close to this point of time, as it is shown in Figure 9. Also the time uncertainty of detection by PMTs, which is represented by a gaussian, takes part in this function and so it is a convolution of the two functions. The x-axis represents the time of delay and y-axis shows the probability for this value to appear in an emission spectrum of photons. Since a delay is supposed to extend the time t_s – and thereby t_j –, the negative time values are actually positive in time. This is considered in Equation 25 by giving t_s a negative sign. In Figure 8, one can observe, this function dominates the principle probability distribution of isochrones as long as the spatial detection efficiency $\epsilon_j(x)$ for a PMT is not taken into account.
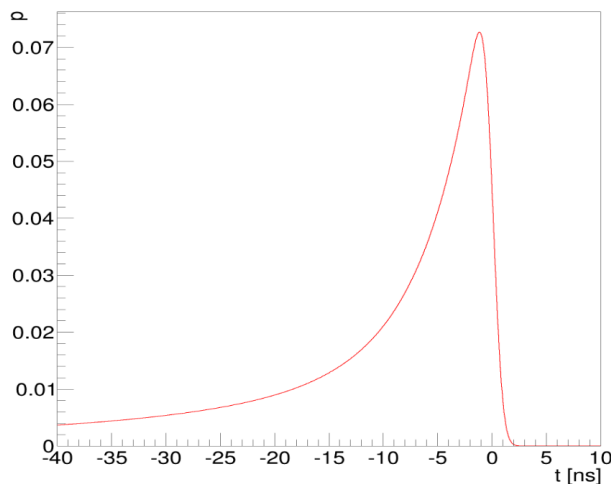

Figure 9: This panel shows the time distribution in photon emission of the scintillator components convoluted with the time uncertainty of PMTs, which is a gaussian of 1 ns standard deviation [19].

4.2 Probability mask and iterations

A probability mask adds information to the previous outcome for the spatial density function $\Gamma_{em}(\mathbf{x})$, which represents the three dimensional topology of an reconstructed event. Thereby such a mask improves the precision of a subsequent iteration step.

An information could be a prior knowledge about the actual spatial distribution of an

event. This would be a spatial mask $M(\mathbf{x})$. The mask gets multiplied with normalization factor and therefore the new spatial probability density function is

$$\Phi_{j,k}(\mathbf{x}) = w_{j,k} M(\mathbf{x})\epsilon_j(\mathbf{x}) \int_0^\infty \Phi_{t_s}(\Delta t)\Phi_{t_{ph}}(t'; \mathbf{x}, \mathbf{r_j})dt' \quad . \tag{31}$$

Consequentially the new normalization is

$$w_{j,k}^{-1} = \int_{V_{LS}} M(\mathbf{x})\epsilon_j(x) \int_0^\infty \Phi_{t_s}(\Delta t)\Phi_{t_{ph}}(t'; \mathbf{x}, \mathbf{r_j})dt' dV \tag{32}$$

The goal of subjoining such information is, to reduce inaccuracies within reconstruction, which get induced by mistakenly measured photons, emerging from dark noise[5] and scattered light. Latter could originate from a point, that definitely was not part of the event, hence the value $M(\mathbf{x})$ turns out to be small for this position $\mathbf{x}$. That implicitly means, $M(\mathbf{x})$ has low values or value zero for points $\mathbf{x}$ outside the mask.

In principle such a mask can be set arbitrary or can be a previous result of any reconstruction method. The most interesting way is to create such a mask out of the reconstruction result of the actual reconstruction algorithm. For example, one can proceed a first reconstruction without any mask. The outcome can be transformed in a mask and subsequently be used for a new reconstruction calculation, referred to as iteration. The new result can also get formed into a mask for a next iteration, etcetera. Each iteration can thereby use a finer spatial segmentation than the previous, which leads to better localized results with improved spatial resolution.

---

[5]Signals, not caused by any events of interest but background.

5 Electron- and positron-discrimination

This section will introduce the principle of the discrimination method using the concept of Negative Photons. Additionally, it will list every conceptual step with mathematical and textual descriptions in the same order, the method walks through while it proceeds.

5.1 The discrimination principle

The discrimination principle focuses on the two occurring gammas in positron events. Besides the main signal source on the event vertex, these photons can result in a second and third source of signals during the reconstruction of an event. The original event vertex will always be the strongest emission source and both gammas cause emission points, being very weak and very close in space to the vertex (see Figure 11). Therefore, the basic Wonsak Reconstruction will most likely result in only one extended event topology, centered on one point (see Figure 10a). If the two further emission sources, caused by the two gammas, can be made visible on the result picture, it is possible to separate positron events from electron events, since electron events do not result in these three signal sources.

The basic idea for realizing this discrimination is to subtract an artificial event topology of an electron from the reconstructed event topology, using the same overall emission strength as the main event vertex of the actual event topology. In principle the result of this subtraction should show two emission sources very close to the original event vertex for positron events or the result should – in best case – show no emission source, if the event itself was an electron event.

An artificial electron event topology is created by estimating the whole energy[6], that was deposited in this event and subsequently an emission source is built at the original event vertex position. This creates a signal, correspondent to the prior estimated energy minus two times the energy of $0.5\,\mathrm{MeV}$. Subtracting this $1\,\mathrm{MeV}$ accounts for the energy loss of the vertex in the original event, caused by those two emitted $0.5\,\mathrm{MeV}$ gammas in case of positron events.

To obtain such a corresponding artificial emission source, the remaining amount of energy is used to calculate the amount of photons, a detector would expect to register from an event with this energy and only one emission point. The mathematical steps of creating an event like this will be subject of subsection 5.2 and therefore not be elaborated in this section. The following subsubsection 5.1.1 presents results of an idealized application using this strategy.

---

[6]For example one could use a prior reconstruction method.

5.1.1 Discrimination example

A first test, if the previous strategy could lead to successful discrimination, was conducted with a short script, written by Björn Wonsak. This script did not consider any physical effects of photons in a liquid scintillator, but the delaying of photon emission according to Figure 9. Furthermore this code was not implemented into the official Wonsak Reconstruction and had its own idealized but appropriate reconstruction algorithm. Hence, it was capable of testing the idea in an idealized environment[7], but not of proving its use within the actual reconstruction algorithm.

The subsequently used pictures are not normalized, i.e. the colors just indicate high and low probabilities but do not represent actual probability values. Figure 10 shows the reconstruction result of an ideal positron event (left panel; which was also an artificially, but not simulated, event) in the detector as well as the artificial electron event (right panel), also referred to as electron hypothesis.

The x- and y- axes represent a two dimensional space in arbitrary units, whereas the colors show the height of local probability density $\Phi(\mathbf{x})$, with yellow colors for high values and blue colors for low values in arbitrary units. The probability values in the right panel are inverted, being negative, so one can superpose the left and right panel by addition.
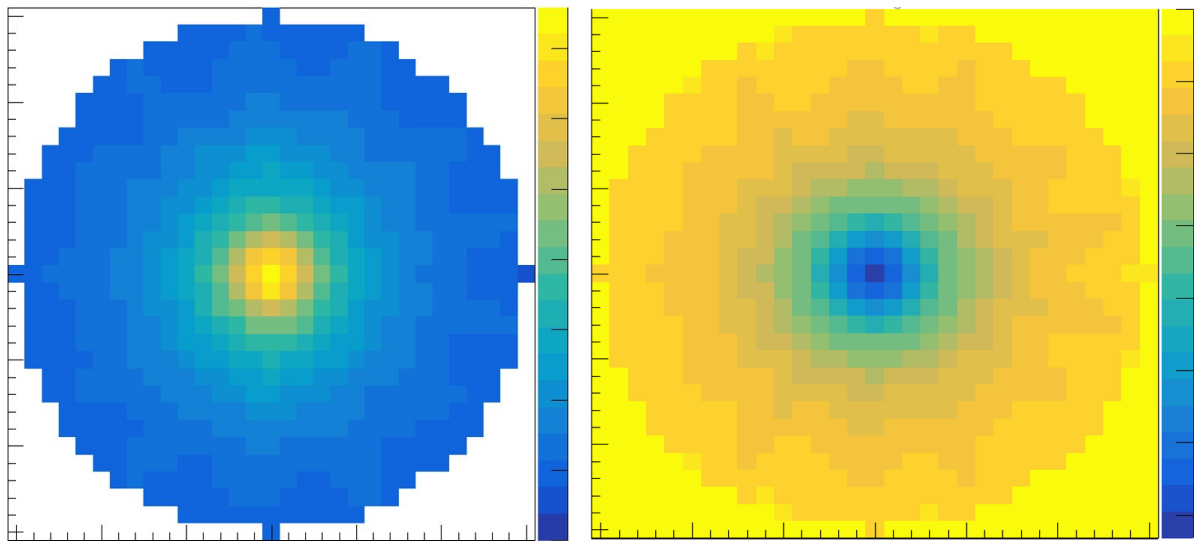
(a) Idealized event topology of a proton event.   (b) Inverted electron hypothesis

Figure 10: This figure shows the ideal event topology of a positron event (left panel) and the corresponding inverted electron hypothesis (right panel), which is to subtract from the positron topology. The x- and y-axes represent the two dimensional detector and the colors represent the probability density $\Phi(\mathbf{x})$, for $\mathbf{x}$ being a point within the a detector area. Yellow indicates high values for $\Phi(\mathbf{x})$ and blue stands for low values.

It is recognizable, that Figure 10a and Figure 10b do almost look like the actual same but inverted event. Once these results get superposed, they will lead to Figure 11.

---

[7]This environment just took into account a photons delayed emission from emission points and the travel time.

Axes and colors of Figure 11 are assigned like in Figure 10.

Since the examined event was a positron event, the difference consists of two remaining emission sources, which occur due to the positron annihilation in positron events. They are furthermore at exactly the positions, in which they were set to be, while creating this artificial positron event. If Figure 10a was not representing a positron event but an electron event, these extra emission points would not emerge as the difference. Figure 11b represents this case for this example event. It is clearly visible, that no specific emission point can be made out but just a confuse difference remains, even reaching negative values caused by the subtraction process. The confusion's probability representing values are of negligible height – max value of Figure 11a is 5.0 and in Figure 11b it is 0.5 – and therefore the result is sufficient to recognize it as electron event. The better negative photon's properties align to real physical behavior of signal photons, the better is the annihilation expected to work out within the real reconstruction algorithm.

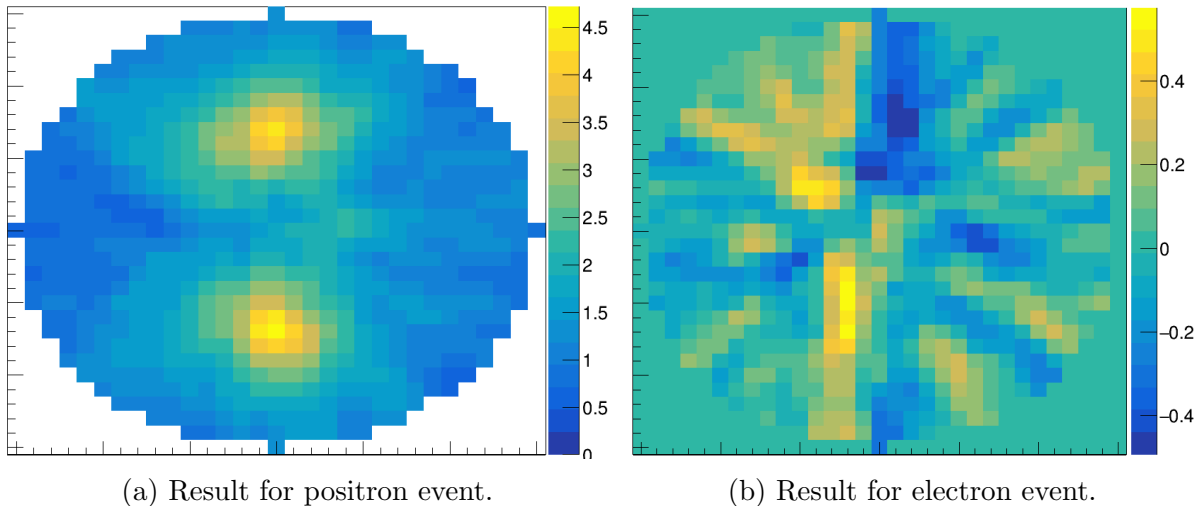(a) Result for positron event. (b) Result for electron event.

Figure 11: After building the superposition of Figure 10a and Figure 10b, the only emission sources remaining are the ones, caused by the two emitted gammas Figure 11a. Such a picture, would be the ideal result of applying the introduced discrimination method. But if the original event Figure 10a, would have been an electron event, the artificial event would most roughly annihilate the original event (Figure 11b). The x- and y-axes represent the two dimensional detector and the colors represent the probability density $\Phi(\mathbf{x})$, for $\mathbf{x}$ being a point within the a detector area. Yellow indicates high values for $\Phi(\mathbf{x})$ and blue stands for low values.

Eventually, this test could prove, the basic idea of discrimination between positron and electron events, using an electron hypothesis subtracted from an positron-/electron-event on position of its main vertex, can work out. The next section will present, how this strategy was implemented into the actual Wonsak Reconstruction algorithm.

5.2 Implementation into Wonsak Reconstruction

This section will present the structure in which artificial events – the mentioned electron hypothesis or also called negative photon event – are created within the Wonsak Reconstruction.

The name concept of negative photons does not refer to photons with negative properties in any physical context, but was chosen for artificial events, since their photon signals will get subtracted mathematically from the actual event signal and therefore it can be seen as a negative photon event. In the Wonsak Reconstruction, a photon, that was detected by any PMT, gets assigned two distinct properties. First property of every photon is the signal time, which is, within this method, the time, a photon used to travel from its emission point $\mathbf{x}$ to the detecting PMT at $\mathbf{r_{ref}}$. The second property is called charge and indicates, if the reconstruction treads the considered photon as one actual photon (corresponding to the charge value one) or as a photon, that does just count as the fracture of one photon, wherefore multiple photons, having different signal times and a charge less than one, can get treated equal one photon. For normalization reasons the concept of negative photons will almost every time treat an artificial photon as one with less charge than one and distribute many such to one PMT until it has the total negative photon charge of one. This way makes it easy to find one universal factor, every PMT's charge can multiplied with. This results in giving every PMT the exact same number of negative photons – spoken of the summed photon charge – which is necessary in an interim stage of this method.

Although a detailed list of steps is provided in its order of implementation subsequently, it follows a first overview about the procedure. The implemented method first figures out, what time a photon, emitted from the actual vertex, needs to travel through the liquid scintillator to a PMT. Furthermore it assigns a detection probability for such a photon's detection to every PMT. In a next step the creation of negative photons starts, using the previously determined propagation time plus the emission time to assign a total signal time to a photon. Also, the time distribution function Φ_{t_s} (see Figure 9) gets used for determining the considered photon's charge, depending on its emission time. Afterwards, in order to take photons scattering into account, these photon's charges get reweighed, so that photons with a higher propagation time get a higher charge. The step is reasonable, since the charge represents the likelihood of measuring a photon with a specific signal time and scattering increases the amount of delayed photons. Hence more delayed photons are detected and delayed artificial photons must have an increased charge. This delocalizes the artifical event in a first attempt, leading to a more smeared probability density in the reconstructed negative photon event (as one can see inFigure 10a an event is never perfectly localized, which has to be considered for any negative photon event as well, in order to annihilate the actual event signal at the vertex position). Now, prior information about the total deposited energy of the event is used to make out the amount

of detected photons, because, in the reconstruction, the amount of photons represent the event energy. Eventually, the individual position of every PMT is used to elaborate, what fraction of the total photons number a specific PMT would detect and consequently its sum of negative photon charges gets reduced or raised. Prior to the last step, every PMT got a certain amount of negative photons, with the total sum of charges equals one, but after taking into account the actual number of detected photons in an event and the position related photon distribution, every PMT gets exact the amount of negative photons, corresponding to the number of photons, the PMT would expect to measure. The last step of the method itself is to save the negative photons with its two properties into a data format, suiting to the format, the reconstruction can use to reconstruct. Depending on the preferred method, there are now multiple ways to conduct the final subtraction. These will be discussed in subsubsection 5.2.7.

Now the actual steps will be presented and for the sake of simplicity, the text will always just consider one PMT and its negative photons. Of course the same procedure is conducted for every single PMT, used in the Wonsak Reconstruction algorithm.

5.2.1 Propagation times

In order to get the propagation time $t_{\text{prop}}(\alpha, L)$, which is the travel time of a photon from its emission point $\mathbf{x}$ to the PMT at $\mathbf{r_{PMT}}$, the distance L between $\mathbf{x}$ and $\mathbf{r_{ref}}$ is calculated and also the angular α of this line to the PMT's surface normal gets resolved. These values are now used to read out the propagation time from a previously and externally built look up table (LUT).

This LUT is depicted in Figure 12, where the x-axis is the distance L in m and the y-axis is the angular α in rad. The colors, explained in the right legend, represent the propagation time in ns. The shape of this LUT represents its constraints, based on the geometrical constraints of the JUNO detector.

5.2.2 Detection probabilities

The same distance L and angular α are now used to obtain the probability $P_{det}(\alpha, L)$, that the PMT detects a photon, originating from this position $\mathbf{x}$. Therefore another LUT, containing these probabilities, gets used, whereby two different LUTs have been considered. One LUT was the result of a simulation for detection probabilities and the other was calculated analytically (Figure 13). Eventually, the calculated LUT was used, since the simulated one had a lack of information for a certain distance to angular relations. The missing values were most likely the result of a simulation with to few simulated photons and therefore, some tuple (L,α) did not get distributed an accurate detection probability.

Figure 13 represents the used calculated LUT. The x-axis represents the distance L in m, whereas the y-axis stands for the angular α in rad. The colors, explained in the right
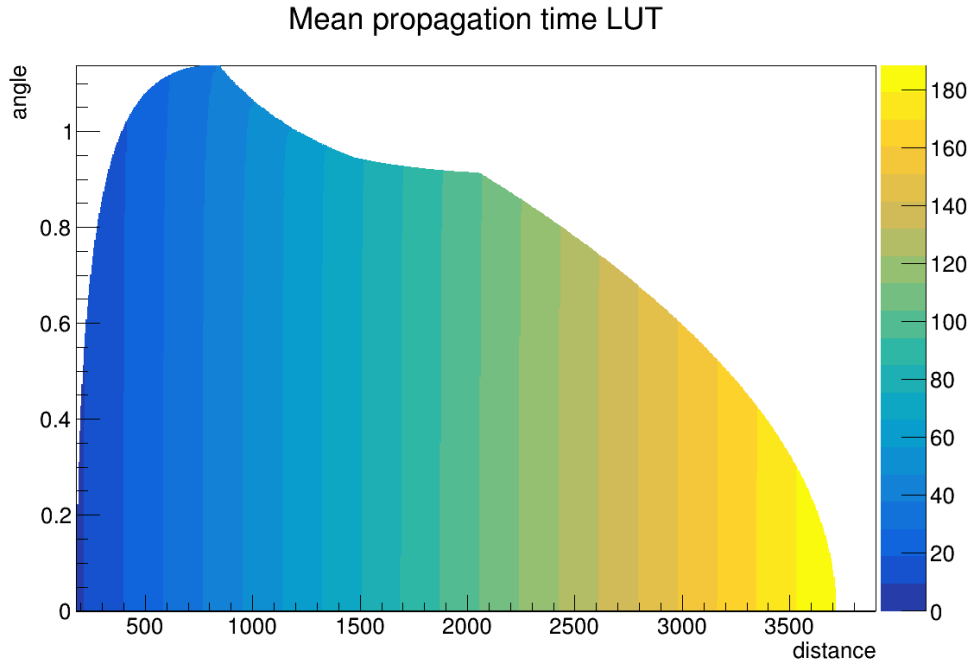
Figure 12: Propagation time $t_{\mathrm{prop}}(\alpha, L)$ LUT. The x-axis is the distance L in cm and the y-axis is the angular α in rad. The colors, look to the right legend, represent the propagation time in ns

legend, give the detection probability $P_{det}(\alpha, L)$. Like in the LUT before, the shape of this LUT represents its constraints, based on the geometrical constraints of the JUNO detector.
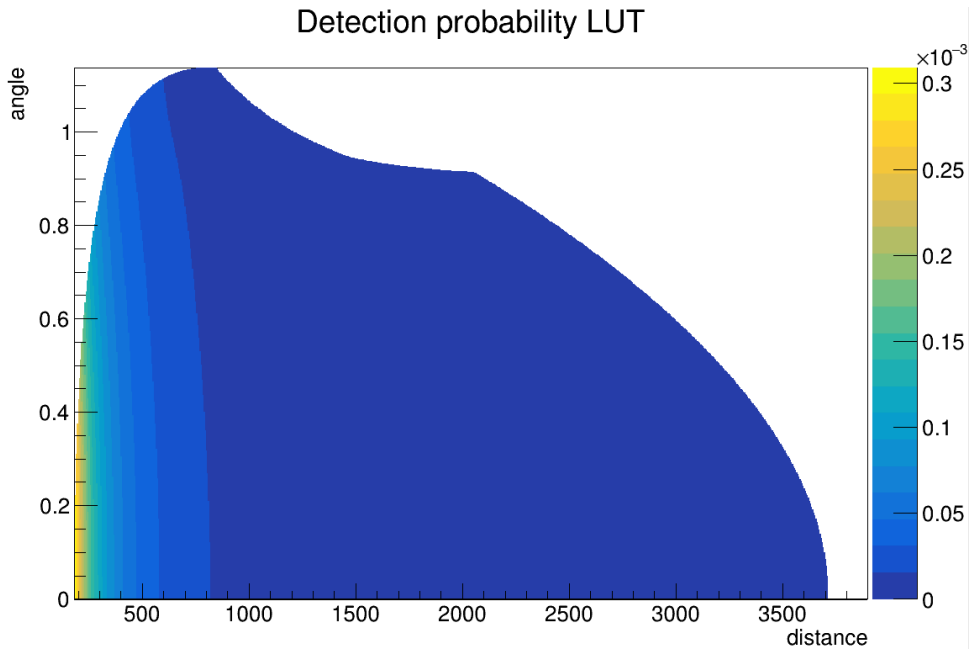

Figure 13: Picture of the detection probability LUT. The x-axis represents the distance L in cm, whereas the y-axis stands for the angular α in rad. The colors, explained in the right legend, give the detection probability $P_{det}(\alpha, L)$.

5.2.3 Creating negative photons

The creation of negative photons already tries to address the issue about smearing the probability density $\Phi(x)$, so that a realistic distribution will be obtained. Hence, a first step of artificial smearing is to create a number N of negative photons, all with different emission times and corresponding photon charge, plus using the propagation time t_{prop} for the same point $\mathbf{x}$. This is done by choosing a time interval, which contains the significant part of the time distribution function Φ_{t_s} (see Figure 9) and create the number N along this time interval, which has the time unit ns. Since a real PMT is just capable of detecting a new incoming photon every kth ns, it is reasonable to create one photon every $1\,\mathrm{ns}$, which is still a rather short and therefore idealized time value. Choosing this time, it is possible to represent the most significant parts of the time distribution function Φ_{t_s} with the emission time t_{delay} of a photon within an interval I for example from -80 to $5\,\mathrm{ns}$, on the time scale of Figure 9. This means, in this case $N = 85$ photons are created for this interval, all with the function value $S(t_{\mathrm{delay}})$ of the time distribution function Φ_{t_s} as charge value. In principle it is possible to choose a greater interval, but every additionally created photon affects the reconstruction time negatively and does not necessarily contribute effectively to the aimed smearing.

Right now, in this moment a PMT gets assigned the N negative photons with their own signal time t and charge C. Time and charge of an ith photon are determined with

$$t_i = t_{\mathrm{prop,i}} + t_{\mathrm{delay,i}} \quad , \tag{33}$$

$$C_i = S(t_{\mathrm{delay,i}}) \quad , \tag{34}$$

with $i \leqslant N$, $t_{\mathrm{prop,i}} > 0\,\mathrm{ns}$, $t_{\mathrm{delay,i}} \in I$ and $C_i > 0$. The charge C_i gets set negative at the end of reconstruction, due to the Wonsak Reconstruction, which accurately works using positive charges.

The sum of photon charges C must fulfil the condition

$$C = \sum_i^N C_i = 1 \quad . \tag{35}$$

This is realized by

$$1 = \sum_i^N C_i \cdot f \iff f = \frac{1}{\sum_i^N C_i} \tag{36}$$

with f as normalization factor, leading to the final normalization

$$C = \sum_i^N C_i \cdot f = 1 \quad . \tag{37}$$

The previous condition is necessary to assure, that later on, when an average amount of N photons has to be assigned to every PMT, one can multiply just one reweigh factor with the charge C_i of every PMT's photon. Until now, a PMT gets the photon charge C of just one photon, but N different signal times t_i and this is what leads to a first smearing of $\Phi(x)$.

5.2.4 Photon scattering

Photon scattering means the physical process, in which a photon first scatters within the liquid scintillator and gets detected afterwards. Hence, such a photon will get registered delayed, compared to a direct photon. Mathematically, the probability of a photon, getting detected with a few ns of delay, raises significantly. Therefore the charge value C_i of late photons has to be raised as well.

This is done by using another LUT, which also uses distance L, angular α and signal time t_i, for providing the probability, a detected photon was scattered before. Since the four dimensional picture of this LUT is not descriptive, it was not introduced as a picture.

Also one has to take into account, just a fractional amount of detected photons were scattered, whereas the others are considered to be direct light. Therefore, two LUTs (Figure 14) were used, indicating, how many percent f_{direct} of the detected photons were direct light. The x-axes represent the distance r (in cm) from event vertex $\mathbf{x}$ to the detector centre and y-axes represent the number of detected photons. The left panel in this figure shows the amount of all detected photons for a simulated event, whereas the right panel just depicts the direct photons. Since just the ratio of both LUTs is of interest within this discrimination method, the actual amount does not influence the result, as the ratio is expected to be equivalent to all other events, using different energies. Finally, the factor f_{direct} is calculated by reading out both LUTs for the same tuple (r,α) and dividing the result of the unscattered LUT (Figure 14b) by the result of LUT, including every detected photon (Figure 14a). In case of the JUNO detector, this LUT uses the distance between the detectors centre and the event vertex point $\mathbf{x}$.

Instead of creating new, delayed photons, the existing photon's charge C_i gets modified and the photon time spectrum with corresponding charges (see Figure 9) changes in a way, which mainly raises the late photon's charge C_i with respect to the relation of direct to scattered light. This all is proceeded without violating condition Equation 35, leading to the new charges $C_{i,new}$ and

$$C_{i,new} = f_{direct} \cdot C_i + (1 - f_{direct}) \cdot C_{i,scat,norm} \tag{38}$$

in which $C_{i,scat,norm}$ marks the ith scattered photon charge after normalization, distributed to it by the LUT. This charge's sum also satisfies the condition

$$C_{scat} = \sum_i^N C_{i,scat,norm} = \sum_i^N \frac{C_{i,scat}}{\sum_i^N C_{i,scat}} = 1 \quad . \tag{39}$$

$C_{scat,i}$ is the ith photon charge before normalization and C_{scat} is the whole charge of scattered photons one PMT gets dedicated. This turns Equation 38 into

$$C_{i,new} = f_{direct} \cdot C_i + (1 - f_{direct}) \cdot \frac{C_{i,scat}}{\sum_i^N C_{i,scat}} \quad . \tag{40}$$

Consequently, summing all single photon charges $C_{i,new}$ will result into

$$C = \sum_i^N C_{i,new} = f_{direct} \cdot \sum_i^N C_i + (1 - f_{direct}) \cdot \sum_i^N \frac{C_{i,scat}}{\sum_i^N C_{i,scat}} = 1 \quad , \tag{41}$$

restoring the state, in which a PMT gets just the charge C of one single photon and still N distinct signal times. The only difference is, the spectrum of photon charges C_i, now features a higher value for especially delayed photons.

The total charge and individual photon charge will subsequently be written as C and C_i again.
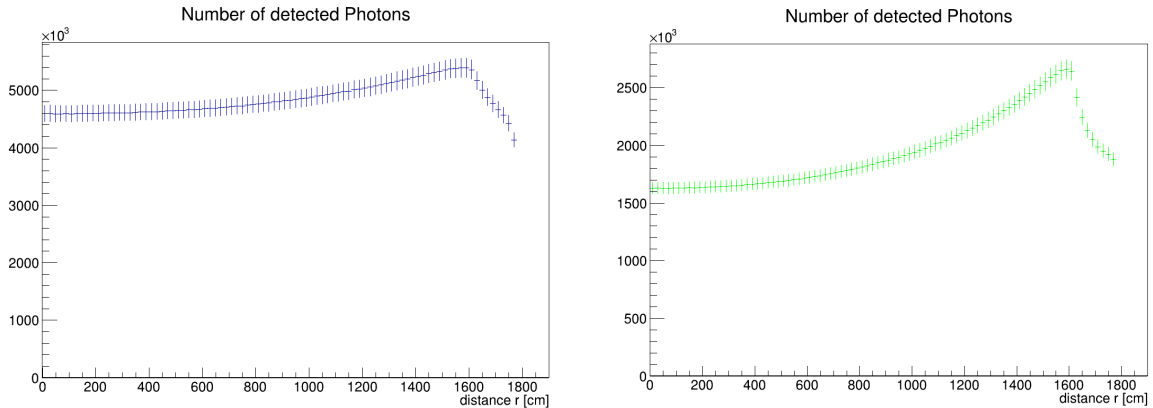
(a) Number of all detected photons, including unscattered and scattered photons.

(b) Number of only unscattered detected photons.

Figure 14: The panels represent a number of all detected and only unscattered detected photons of an simulated event. The number of those photons depends on the distance from event vertex at **x** to the centre of the inner JUNO detector. The x-axis stands for this distance r in cm and the y-axis gives the number of detected photons.

5.2.5 Reweigh photon charge

The total photon charge now has to be reweighed in a way, that every PMT gets the amount of negative photon charge, which represents all detected photons.

This amount can be concluded out of the knowledge about the deposited energy of an event, combined with detector properties. Such properties are the light yield LY of the liquid scintillator (estimated to be 10000 photons/MeV in JUNO) as well as the detection efficency P_{total} (sum of previously determined $P_{det}(\alpha, L)$ per PMT) for the whole detector. The deposited energy has to be estimated via any prior reconstruction method. In best case, the exact energy is known, which is the case for in subsection 5.3 performed reconstructions.

On the way to find out, how many photon charge has to get distributed to each PMT, one has to consider

$$E = E_{est} - 1\,\text{MeV} \quad , \tag{42}$$

$$N_{emit} = E \cdot LY \quad , \tag{43}$$

$$N_{det} = N_{emit} \cdot P_{total} \quad , \tag{44}$$

where E is the estimated energy E_{est} minus $1\,\text{MeV}$ (since an positron event would lose two times $0.5\,\text{MeV}$ to its emitted gammas, which do not cause signals on the main vertex). N_{emit} and N_{det} represent the number of actually emitted and detected photons. Be aware, N_{det} is the amount of total detected photons in the detector with a charge of $C_k = 1$ ($k \in \mathbb{N}$ and $0 \leq k \leq N_{det}$) and the previous used N is the amount of negative photons for a single PMT, with charges unequal one.

Since not every PMT detects the same amount of genuine photons in a real event, but the number of negative photons N is not to be changed for every PMT, one has to readjust the to a PMT distributed negative photon charges C_i. These charges will be changed in a way, that one PMT will get a total charge C, corresponding to the probable sum of charges $\sum_l C_l$ ($l \in \mathbb{N}$ and $0 \leq l < N_{det}$) caused by measured photons.

Therefore, a factor f_C has to be defined and must fulfill the condition

$$N_{det} = \sum_D C_D \cdot f_C \quad . \tag{45}$$

D is the amount of PMTs and the yet used C is defined as $C = C_D = 1$. The total sum of all the charges of all PMTs, will be equal to the number N_{det} of real, detected photons in an event. But every PMT gets an individual charge C, depending on the PMT's detection probability $P_{det}(\alpha, L) = P_D$. Hence, Equation 45 has to be enhanced to

$$N_{det} = \sum_D C_D \cdot f_C \cdot P_D \quad . \tag{46}$$

Finally, the factor f_C can be determined to be

$$f_C = \frac{N_{det}}{\sum_D C_D \cdot P_D} \quad . \tag{47}$$

Now, individual negative photon charges C_i can be multiplied with factor f_C and its probability P_D to be detected, to get the new, final photon charge $C_{i,D}$

$$C_{i,D} = C_i \cdot f_C \cdot P_D \quad . \tag{48}$$

Consequently, every photon charge C_i gets reduced by the probability P_D, leading to the desired ratio of total negative photon charge C to actually detected photon charge for each PMT.

After this step, every PMT has the same amount N of negative photons, with N different signal times. A PMT does not necessary have a total charge C of one anymore and especially does most likely not have the same total charge as any other PMT. So the total charge C of one PMT corresponds to the number of real, detected photons at this specific PMT.

5.2.6 Create PMT-Objects

The final step, after distributing individual negative photons to every single PMT, is to build PMT-Objects. These are objects, the realized Wonsak Reconstruction algorithm uses, to introduce a PMT's properties (such as geometrical or technical information) into itself. Also signal information of detected photons (signal time t_i and photons charge C_i) are treated as properties of every PMT-Object. At first, the so called Hit-Object gets created and filled with the times t_i and charges C_i. This Hit-Object then gets saved into a PmtData-Object, which is a further property of the appropriate PMT-Object.
During the reconstruction process, these PMT-Objects get read out. Further information about the realization of the Wonsak Reconstruction can be get from source [19].

5.2.7 Reconstruction and event subtraction

All negative photon charges C_i were defined to be positive yet. Although they are supposed to be negative, due to the name. These charges just turn out to be negative, as soon as the reconstructed negative photon event gets subtracted from the real event. This

method was a choice of implementation and negative charges could be defined as negative values as well. But then, the reconstruction results just would have to be added instead of subtracted, which – in principle – ends up in the same result. Additionally, the Wonsak Reconstruction was realized without considering negative photon charges, wherefore multiple functions within the reconstruction process might not work as expected. After every step of iteration, one can take a look at both reconstruction results, the negative photon event and the normal event as well as at the result of subtraction.

5.2.8 Probability masks for further iterations

In further iterations, the negative photons use the same probability mask as the examined event in every following step. This way the negative photon signal does not result into a complete different topological signature, deviating too much from the original event vertex.

5.3 Reconstruction results and analysis

This section discusses gathered results of the discrimination algorithm. The first step is to check, if a negative photon event is able to annihilate a point-like event (subsubsection 5.3.1), which is also matches the signal structure of an electron event. To prove the spatial smearing of negative photon events, the second step examines the statistical probability distribution $\Phi(\mathbf{x})$ over the detector radius for simulated events and a negative photon event in the detector centre. As a last step, the algorithm is applied to a 11 MeV positron event, also in the centre.

All used events were simulated via Monte-Carlo Method for the JUNO detector, i.e. no measured data was used, since the experiment is yet to finish construction. Also, the simulated data did not include Cherenkov light, which is why the discrimination method does yet not consider Cherenkov light. The reconstruction algorithm itself did not make use of its own implemented scattered light algorithm and the results were obtained using the emitted light algorithm. The scattered light algorithm assigns a probability to each measured photon to be unscattered, which improves the event localization. Exact explanation can be found in source [33]. The emitted light algorithm, within the Wonsak Reconstruction, reconstructs the event in a way, that the result of probability density represents all emitted and not only detected photons. A further function, smearing the vertex $\mathbf{x}$, was not used as well.

If a reconstruction was proceeded, using a different configuration, it is mentioned in the concerned section.

5.3.1 2 MeV point-like event annihilation

Since the main emission source in an event is point-like, no matter if it is an electron or positron event, the first goal is to build a negative photon event, which imitates a single point-like event. The first event, which was tried to annihilate by negative photons, was a simulated event of 2 MeV kinetic energy with a vertex $\mathbf{x}$ on one side of the JUNO detector. The event contained 2947 detected photons and a total charge – summed charges C over all PMTs –, representing the same amount of negative photons, regardless the energy estimation, was created to obtain an ideal result. Furthermore, the volume of the whole detector was used for reconstruction, segmented into 50 cm cubes. These cubes will represent one probability value within a reconstruction result and can set to smaller sizes in order to improve the spatial resolution. But this raises the computing time significantly and is not necessary within this test.

The time distribution function in Figure 15 represents all therefore created 121^8 negative photons with their own $t_{\mathrm{delay,i}}$ and C_{i}. The x-axis shows the time of delay in ns, whereas the y-axis indicates the number of photons, which represents the charge. This time

---

[8]All these photons do have a very small charge C_i and do not count to the mentioned 2947 negative photons. But their individual charges summed up over all PMTs do represent this total amount.

distribution function is – compared to Figure 9 – inverted. The inversion is chosen, since these times shall represent actual time delays, based on the time distribution function. This is why they are supposed to be positive for most of the created photons. The not inverted version, used within the implemented discrimination algorithm, would cause highly weighed (high negative photon charge C_i) early[9] negative photons, although this function is supposed to represent the time delay.
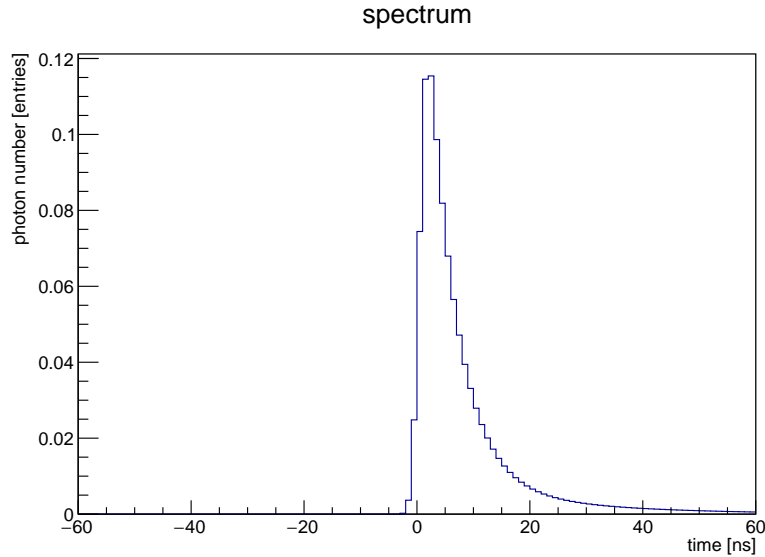

Figure 15: Time distribution function, used to create 121 negative photons with bin width of 1 ns and without propagation time. Normalized to an integral of one. The x-axis shows the time of delay $t_{\mathrm{delay,i}}$ in ns, the y-axis indicates the number of photons with considered delay, which represents the charge C_{i}.

The next step is to add a mean propagation time $t_{\mathrm{prop,i}}$ to every created photon for each PMT individually. Figure 16 shows the resulting time distribution for a PMT after adding propagation time, which is the closest Figure 16a and the farthest Figure 16b to the event vertex. In case of the closest PMT the distribution gets less shifted in positive direction of the time axis compared to the distribution for the farthest PMT.

Now the photon scattering gets applied, which rises the charge of delayed photons according to Equation 38 and thereby reduces the charges of rather early photons. This results into Figure 17 for the time distribution function only and into Figure 18 for photons with travel time to the closest and farthest PMT.

---

[9]Photons in and close to the peak in Figure 9 could be referred to as early, since they have small time values compared to the depicted positive time spectrum.

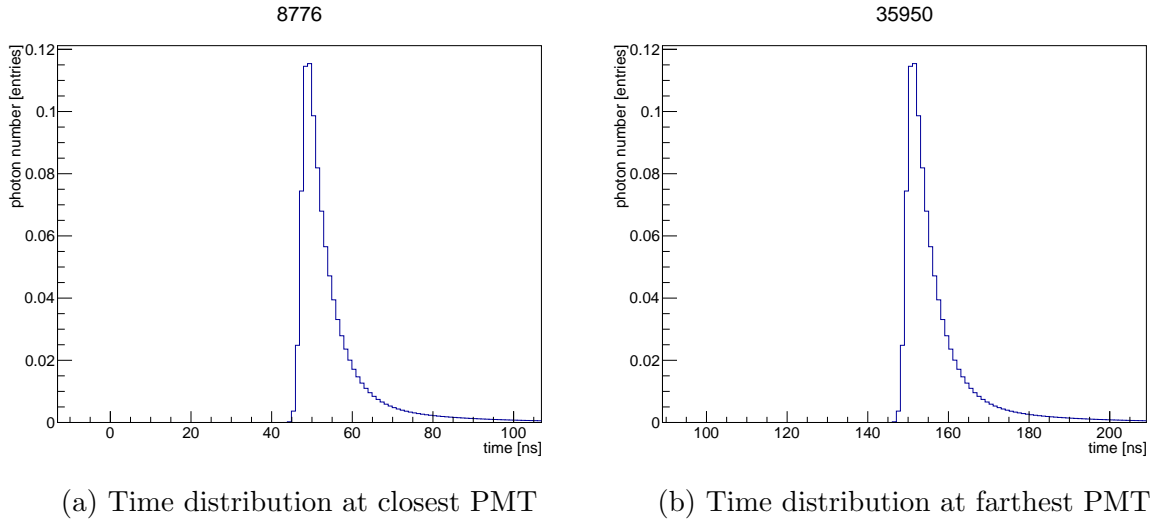(a) Time distribution at closest PMT   (b) Time distribution at farthest PMT

Figure 16: Time distribution function, used to create 121 negative photons with bin width of 1 ns. This time, the propagation time included. Normalized to an integral of one. The x-axis shows the time of delay $t_{\text{delay,i}}$ in ns, the y-axis indicates the number of photons with considered delay, which represents the charge C_i.

Until now, the time distributions react like expected, leading into the reconstruction results Figure 19, Figure 20 and Figure 21. In these pictures, the x,y and z axes represent the spatial dimensions of the detector in m, with the detectors centre set as origin. The colors show the spatial distribution of the probability density $\Phi(\mathbf{x})$, where yellow indicates high probabilities and blue low probabilities (notice the legend on each panel). This probability is not normalized.

The negative photon event imitates the original signal widely as it was expected in order to annihilate it as far as possible. Still, one may notice differences of the probability densities, observing the blue areas within the right and left panel in Figure 19 and Figure 20. The negative photon event results in approximately smooth ellipses, whereas the original event does not. This exposes differences in distributing photon signals to PMTs in a simulated and in a negative photon event. Within the simulation, a PMT gets the amount of photon signal depending on physical statistics, causing unpredictable behavior of such ellipses edges. On the other side, the negative photons get distributed to PMTs steadily, without statistical fluctuation, just depending on detector's properties and the event position.

Subtracting the results, ends in Figure 21. Comparing the pictures and legends, it is visible, the original event did not get annihilated completely. The reconstruction algorithm provides the integral of both events in arbitrary units. 2.287 is the integral of the original event and 2.184 the integral of the negative event. A difference of 0.104 remains, which is 4.5% of the original event volume. The main emission source got reduced far reaching, but some anomalies remained near the constraints of the detector, which is probably caused by a malfunction of the reconstruction algorithm, combined with a not perfect imitation. This malfunction is known and yet to fix. It is to observe in all reconstruction images
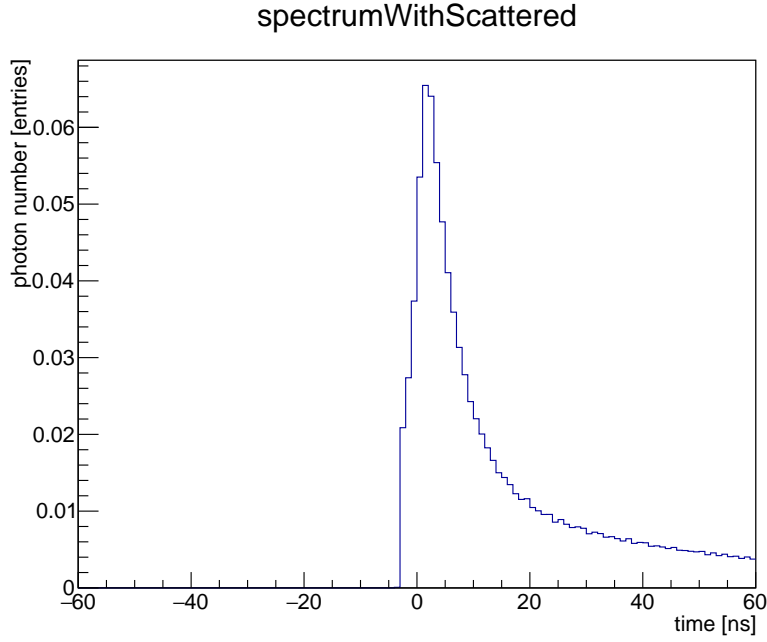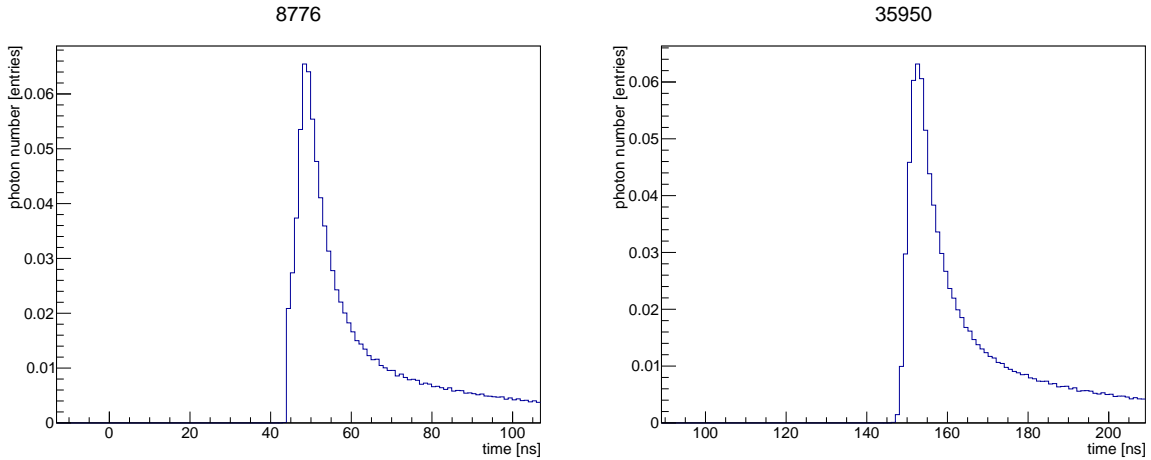
Figure 17: Time distribution function plus scattering, used to create 121 negative photons with bin width of 1 ns and without propagation time. Normalized to an integral of one. The x-axis shows the time of delay $t_{\text{delay,i}}$ in ns, the y-axis indicates the number of photons with considered delay, which represents the charge C_i.

(a) Time distribution at closest PMT

(b) Time distribution at closest PMT

Figure 18: Time distribution function plus scattering, used to create 121 negative photons with bin width of 1 ns. This time, the propagation time included. Normalized to an integral of one. The x-axis shows the time of delay $t_{\text{delay,i}}$ in ns, the y-axis indicates the number of photons with considered delay, which represents the charge C_i.

(compare Figure 19, Figure 20, Figure 21) and effectively drags the spatial probability density into the direction of the detector walls, away from the original event vertex **x** (red dot), once this vertex is not in the detector centre. These anomalies are clearly to localise on sight in the left and right panel of Figure 21. The panel in the middle represents the event projection plane, which is would be seen, looking from the right side of the right picture or looking from the top onto the left panel. This means, the yellow remainder is
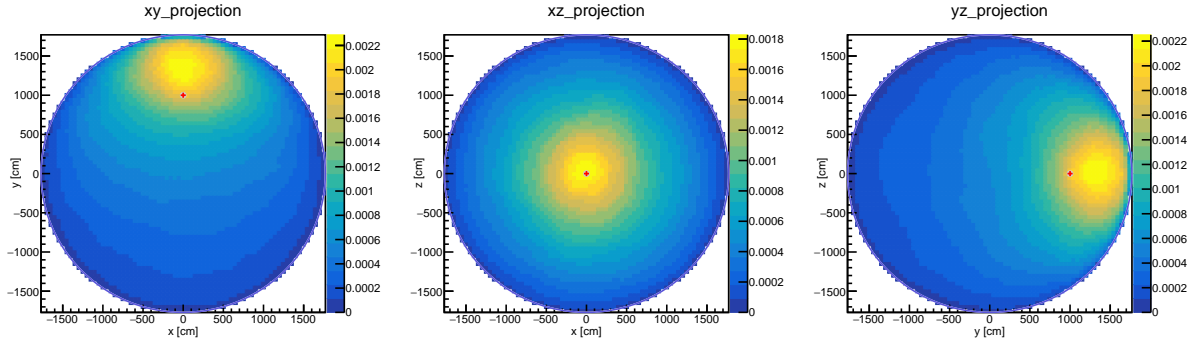
45

Figure 19: Reconstruction result for the original event. The axes x,y and z show the three spatial dimensions of the JUNO detector in cm. Colors represent the not normalized probability density function $\Phi(\mathbf{x})$ with its legend on the right side. The red dot shows the original event vertex $\mathbf{x}$.
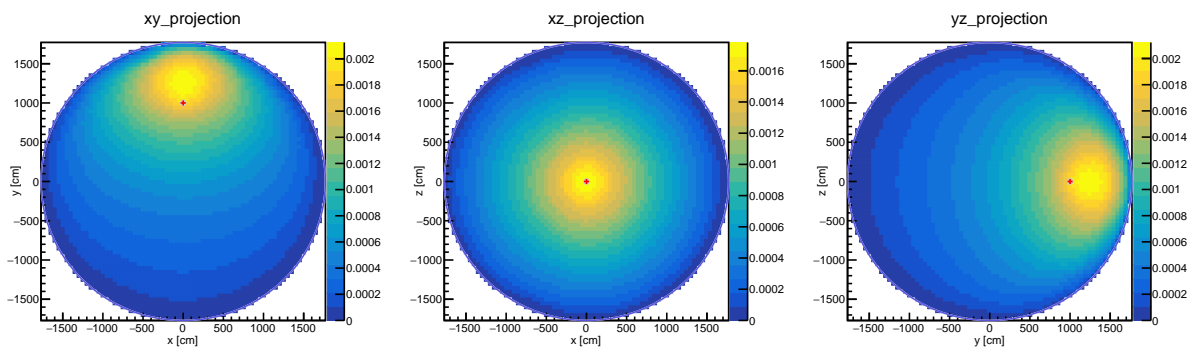

Figure 20: Reconstruction result for the negative photon event. The axes x,y and z show the three spatial dimensions of the JUNO detector in cm. Colors represent the not normalized probability density function $\Phi(\mathbf{x})$ with its legend on the right side. The red dot shows the original event vertex $\mathbf{x}$.

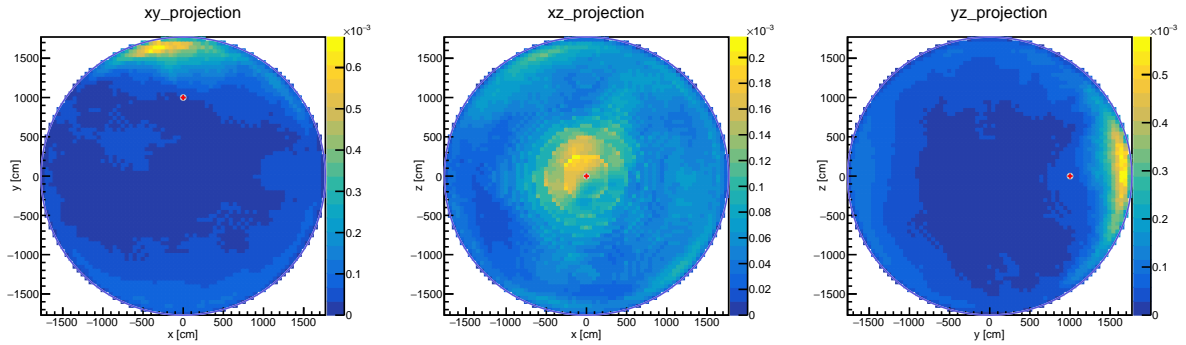still localised on the detectors constraints and could not get canceled out by the negative photon event.

Figure 21: Result for subtraction of the reconstructed negative photon event from the original event. The axes x,y and z show the three spatial dimensions of the JUNO detector in cm. Colors represent the not normalized probability density function $\Phi(\mathbf{x})$ with its legend on the right side. The red dot shows the original event vertex $\mathbf{x}$.

Given the perfect fitting number of negative photons, the negative event seems to cancel out a simulated event in a not perfect but good manner.

5.3.2 Radial signal distribution in point-like events

The distribution of negative photon signals to PMTs also depends on the vertex position **x**, but provides a smooth distribution of photon charges C over all PMTs. This corresponds to a smooth photon distribution of simulated events. Like in subsubsection 5.3.1 described, a simulation as well as a real event, would not cause a such smooth distribution. Some PMTs would measure less or more photon signals than expected. This process potentially impedes electron positron discrimination by not respecting significant fluctuations in single events.
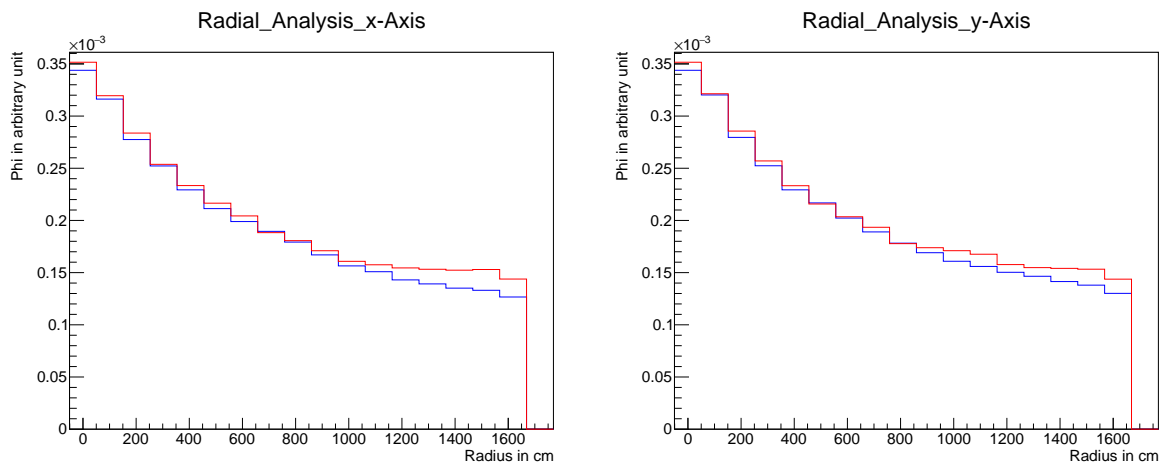
(a) Probability density over radius along direction x

(b) Probability density over radius along direction y
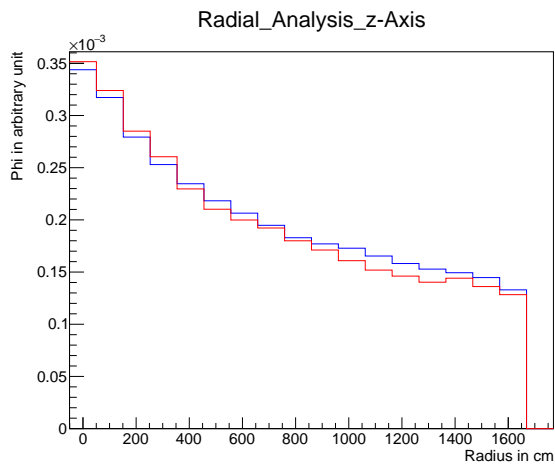
(c) Probability density over radius along direction z

Figure 22: These histograms indicate the radial distribution of the probability density $\Phi(\mathbf{x})$ (y-axis in histogram) over the detector radius (x-axis in histogram) along the different spatial axes x,y and z in in cm. The detector's centre is set to be the origin in space and the event vertex **x**, which is equal to radius zero. The distribution is the average result of 96 simulated 3 MeV events (blue) plus 1 negative photon event (red).

Furthermore, the discrimination relies on the LUTs (see subsection 5.2) for propagation time, detection probability and photon scattering. Especially the scattering LUT is

supposed to lead to a realistic spatial distribution of the negative photon's probability density, wherefore the discrimination is very sensitive to the accuracy of this LUT. This LUT is the result of a scattering simulation, using our own model for scattering and depends on the precision of the physical model. In contrary, the event simulation proceeded with Geant4. The LUT's accuracy was tested by simulating 96 point-like events of 3 MeV kinetic energy, located in the detectors centre, reconstructing them and examining the probability distribution $\Phi(\mathbf{x})$ along the detector's radius. This distribution was subsequently compared to the distribution, one negative photon event creates along the same radius. A single negative photon event underlies almost non fluctuation, since their properties do not depend on random number generators and is therefore already able to represent larger statistics in an good approximation. With this comparison, the quality of the scattering LUT and the whole process of smearing was estimated.

The reconstruction used 100 cm cubic segmentation of the detector's whole volume and reconstructed, using every kind of PMT. It furthermore proceeded only one step of iteration and created 120 negative photons per PMT with 1 ns width, summing up to a total charge for the detector equal to 4125 photons. This is the amount of photons, which was detected in the simulated events. Figure 22 shows the resulting probability density $\Phi(\mathbf{x})$ in average for the 96 simulated events in blue. The histogram's x-axis represents the radius of detector in the directions of x,y and z in cm. The y-axis indicates the probability in arbitrary units.

The red histogram represents the distribution of the negative photon event. In general both distributions show a similar progression with the biggest differences in all three directions appearing between the radius range of 900 cm to 1650 cm. This systematic deviation indicates a still not perfect signal imitation by the negative photons, wherefore some alignments at the used LUTs could improve the quality of imitation. In general, this differences should still allow discrimination in low energy sector around 2 or 3 MeV, because the positron gammas produce a 0.5 MeV signal, which in this case would still have a big contrast.

Moreover, the distribution of a single positron event of the previous 96 compared to the same negative photon event is shown in Figure 23. Although the same number of photons got detected within the simulated and the negative event, both distributions are still not identical. The negative event always reproduces higher values between the radius origin and 600 cm, whereas the relation for the second half of the radius differs, considering the three directions and finer segments of the radius. The superposition of those reconstructed events would produce negative values of probability density at the vertex position.
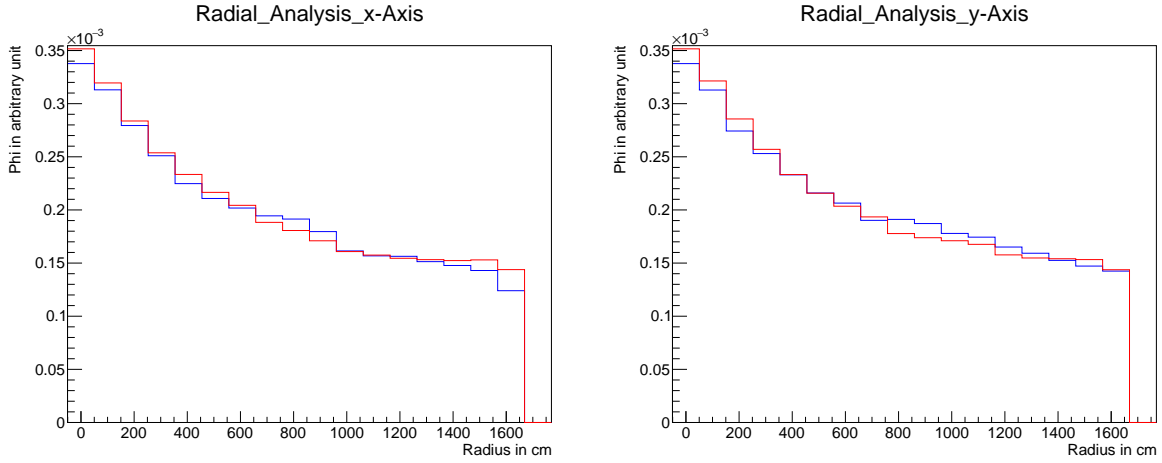
(a) Probability density over radius along direction x

(b) Probability density over radius along direction y
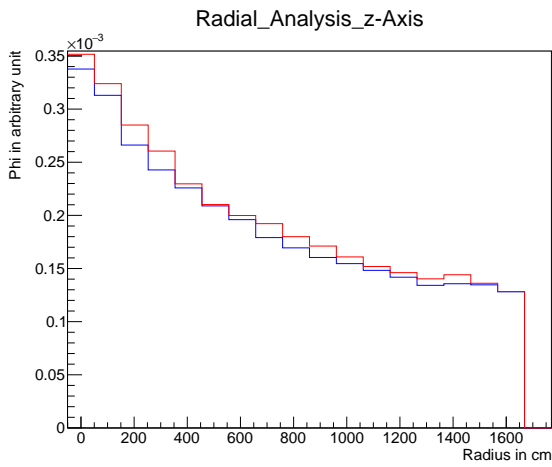
(c) Probability density over radius along direction z

Figure 23: These histograms indicate the radial distribution of the probability density $\Phi(\mathbf{x})$ (y-axis in histogram) over the detector radius (x-axis in histogram) along the different spatial axes x,y and z in in cm. The detector's centre is set to be the origin in space and the event vertex $\mathbf{x}$, which is equal to radius zero. The distribution is the result of one single simulated 3 MeV event (blue) plus 1 negative photon event (red).

5.3.3 11 MeV positron event

The discrimination method was now tested on a simulated 11 MeV positron event in the centre of JUNO. Therefore, three steps of iterations were chosen with different cube sizes and the space of reconstruction within the detector was reduced to a sphere of 300 cm diameter. The algorithm created 121 negative photons with the time width of 1 ns (compare Figure 15). In this step of reconstruction, the energy estimation was used to determine the total amount of negative photon charge. Instead of using a pre-reconstruction method to estimate the events energy, the exact value was set to 10.5 MeV, since no reliable energy reconstruction method was available. The given energy estimation was chosen to a lower value than 11 MeV, since the estimation algorithm tends to predict slightly higher photon

50

numbers, than the initial event contains. Moreover, a discrimination is also supposed to work, if the exact energy deposition was not estimated appropriately. However, the total photon charge was estimated to an equivalent of 14757 photons, whereas the original event contained 17344 photons. A fraction of the difference is caused by the photons, emitted by the two 0.5 MeV gammas. The final cube sizes for the iterations were 100 cm, 50 cm and 25 cm. This led to the results Figure 24 and Figure 25.

The red dot in the middle of each panel represents the event vertex and the end of the black lines shows, where exactly the two gammas caused their additional emission sources. Despite the difference of nearly 2500 photons, the maximum values of both, the original event as well as the negative event, are close with a deviation of 9% and the negative photon event having the highest value. This confirms the statistical experience of the, in Figure 22 shown, behavior. Apart from that, the overall probability distributions of both events seem to be nearly similar.
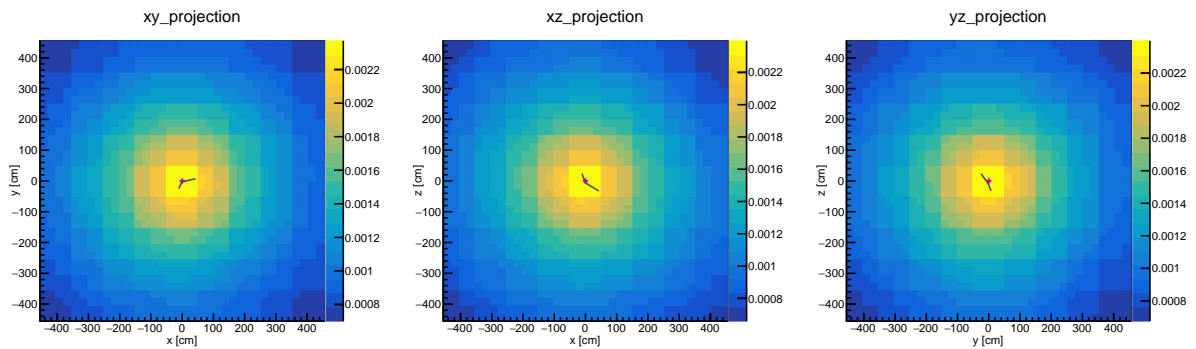

Figure 24: 11 MeV positron event: Reconstruction result for the original event. The axes x,y and z show the three spatial dimensions of the JUNO detector in cm. Colors represent the not normalized probability density function $\Phi(\mathbf{x})$ with its legend on the right side. The red dot shows the original event vertex $\mathbf{x}$ and the end of the black lines show the additional signal sources of the two gammas.

Figure 25: 11 MeV positron event: Reconstruction result for the negative photon event. The axes x,y and z show the three spatial dimensions of the JUNO detector in cm. Colors represent the not normalized probability density function $\Phi(\mathbf{x})$ with its legend on the right side. The red dot shows the original event vertex $\mathbf{x}$ and the end of the black lines show the additional signal sources of the two gammas.
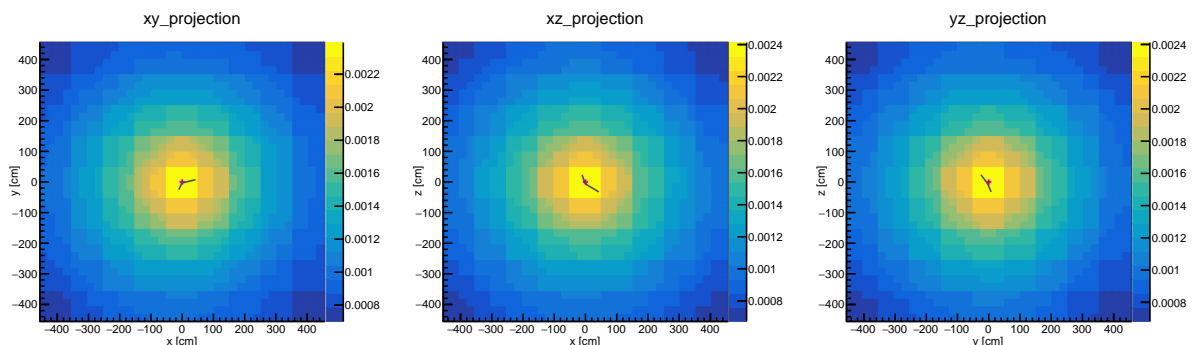
Figure 26 represents the result after subtraction. Its integral in arbitrary units is 0.0041, whereas the integrals of the normal event is 1.542 and the negative photon event has 1.538. The result pictures do not display the desired structure, as it was reached with the test in subsubsection 5.1.1. It is not clear, if the structure of the remains corresponds to the two gamma signals. Although the rest signals seem to align to the orientations of the black lines. If it was caused by the gammas, one can argue, that the distribution got dragged into one direction, away from its original sources, because the reconstruction uses to drag the distribution to a side (compare Figure 19). But the remainder could also be explained by fluctuations of the simulated event result. To make out the origin, one has to proceed a certain amount of reconstructions, applying the algorithm, with a finer spatial resolution and observing the statistic behavior. Unfortunately, there was not enough time, to realize such a statistic within the time frame of this thesis.
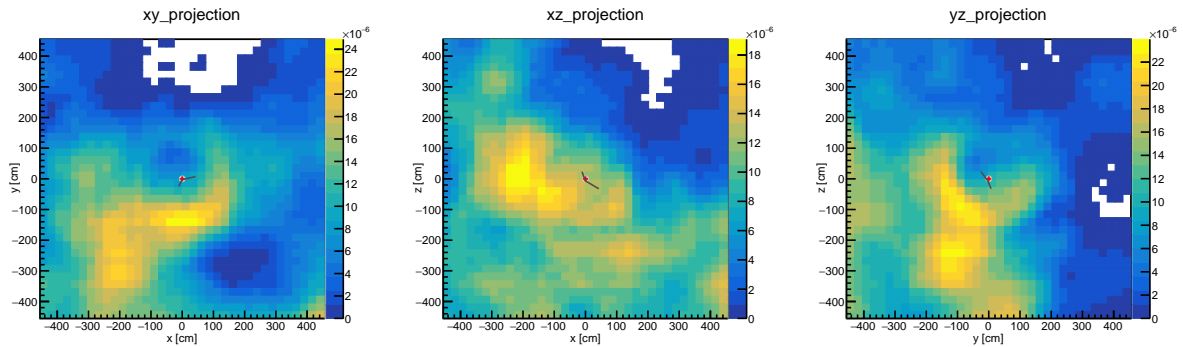

Figure 26: 11 MeV positron event: Result for subtraction of the reconstructed negative photon event from the original event. The axes x,y and z show the three spatial dimensions of the JUNO detector in cm. Colors represent the not normalized probability density function $\Phi(\mathbf{x})$ with its legend on the right side. The red dot shows the original event vertex $\mathbf{x}$ and the end of the black lines show the additional signal sources of the two gammas. White space indicates negative probability values, which did not get displayed.

6   Conclusion

The implemented discrimination method, using the concept of negative photons, was running successfully as an enhancement of the official reconstruction algorithm. The artificially created negative photons were able to show the exact same behavior as photons, which get injected into the reconstruction from simulated events.

Such a negative event was furthermore capable of annihilating an electron event. Although, it was not able to make the two emitted gammas on positron events clearly visible, it is still an interesting candidate for electron and positron discrimination within the Wonsak Reconstruction, as both algorithms will be evolved in future.

In a first approach, it was able to annihilate a point-like event, equal to an electron event, leaving a few remainders of raised probability values close to the event centre. Despite the minimum of differences, these remainders can negatively affect discrimination, since in certain cases it may not be clear to a final stage, if such remainders can overlap existing gamma signals in positron events in a way, that these sources get hidden and the event misinterpreted. These remains are most likely statistical fluctuations occurring during events. In order to address these fluctuations, one has to figure out and study the statistical behavior, which might be impeding the discrimination algorithm. Also enhancing the scattered light adjustment to the negative photons can be reconsidered, for example by checking the correctness of the used LUT.

A radial probability density analysis of point-like events in the detector centre has shown, that the radial distribution of simulated and negative photon events differ slightly in some regions. But its progression was still very similar for negative and simulated events, already leading to good results in sense of realistic event smearing.

Despite the implemented algorithm works quite reliable and stable, a bug appeared within the algorithm. It occurs, once small PMTs get deactivated within the reconstruction algorithm. It leads to a major lack of negative photon signals, although these PMTs measure a rather negligible fraction of detected photons in simulated events. This bug occurs, although the detection probability P_D reduces the amount of assigned negative photons significantly for small PMTs (compare Equation 48). It is to expect, that this issue can get fixed within one careful search.

Since there was not enough time remaining to test it, a reasonable next step must be to construct an unrealistic positron event, placing the gamma signal sources in magnificent distances to the vertex. In an realistic simulated event, these additional sources are localized in close range to the vertex, meaning distances of about 40/,cm. By testing such an artificial event, one will clearly figure out the behavior of these additional signal

sources within the reconstruction and after applying the discrimination. This knowledge will make it easier to interpret even the results of simulated positron events.

Both, the issues about occurring fluctuating remainders and the radial deviations, can be examined in future by building up larger statistics. It would be reasonable to reconstruct a large amount of events and compare their fluctuations and radial distributions. These events could be placed in the centre. An equal amount of electron, positron and their belonging negative photon events, all depositing and emitting the same energy on the main vertex, could lead to a better statistical understanding of how to adapt the properties of negative photons. In such a way one can figure out, how significantly fluctuations of these events impede the discrimination and how the remainders of positron events correspond to the gammas.

7 Bibliography

[1] Aartsen, M. G. et al. "Development of a General Analysis and Unfolding Scheme and Its Application to Measure the Energy Spectrum of Atmospheric Neutrinos with Ice-Cube." The European Physical Journal C 75.3 (2015): n. pag. Crossref. Web.

[2] Aartsen, M. G. et al. "Measurement of the Atmospheric ν_e Spectrum with IceCube." Physical Review D 91.12 (2015): n. pag. Crossref. Web.

[3] Aartsen, M. G. et al. "Measurement of Atmospheric Tau Neutrino Appearance with IceCube DeepCore." Physical Review D 99.3 (2019): n. pag. Crossref. Web.

[4] Aguilar, A. et al. "Evidence for Neutrino Oscillations from the Observation Ofν^-e appearance in $\nu^-\mu$beam." Physical Review D 64.11 (2001): n. pag. Crossref. Web.

[5] Aguilar-Arevalo, A. A. et al. "Event Excess in the MiniBooNE Search for$\nu^-\mu \rightarrow \nu^-$e Oscillations." Physical Review Letters 105.18 (2010): n. pag. Crossref. Web.

[6] Amoruso, S. and others: Measurement of the mu decay spectrum with the ICARUS liquid Argon TPC, in The European Physical Journal C, Band 33(2) (2004), 233 - 241.

[7] An, Fengpeng et al. "Neutrino Physics with JUNO." Journal of Physics G: Nuclear and Particle Physics 43.3 (2016): 030401. Crossref. Web.

[8] Bahcall, John N.: Neutrino Astrophysics, New York: Cambridge University Press 1989.

[9] Demtröder, Wolfgang: Experimental-Physik 4 Kern-, Teilchen- und Astrophysik, 5th ed., Berlin: Springer Science+Business Media S.A. 2017.

[10] Ecker, Gerhard: Particles, Fields, Quanta - From Quantum Mechanics to the Standard Model of Particle Physics, Cham (Switzerland): Springer Nature Switzerland AG 2019.

[11] Fengpeng An et al.: Neutrino Physics with JUNO, in J. Phys., G43(3):030401, (2016).

[12] Giunti, Carlo, and Marco Laveder. "Statistical Significance of the Gallium Anomaly." Physical Review C 83.6 (2011): n. pag. Crossref. Web.

[13] Guo Cong, on behalf of the JUNO collaboration: Atmospheric neutrino spectrum reconstruction with JUNO, in arXiv:1910.11172 (2019)

[14] Huber, Patrick. "Determination of Antineutrino Spectra from Nuclear Reactors." Physical Review C 84.2 (2011): n. pag. Crossref. Web.

[15] JUNO Team: Introduction to JUNO, in: JUNO - Jiangmen Underground Neutrino Observatory, 2013, unter: http://juno.ihep.cas.cn/ATEjuno/201309/t20130912_109433.html [last visited: 2019-11-04].

[16] Kuno, Yoshitaka and Okada, Yasuhiro: Muon decay and physics beyond the standard model, in Reviews of Modern Physics (2001).

[17] Kusenko, Alexander. "Sterile Neutrinos: The Dark Side of the Light Fermions." Physics Reports 481.1-2 (2009): 1–28. Crossref. Web.

[18] Li, Yu-Feng. "Overview of the Jiangmen Underground Neutrino Observatory (JUNO)." International Journal of Modern Physics: Conference Series 31 (2014): 1460300. Crossref. Web.

[19] Lorenz, Sebastian: Topological Track Reconstruction in Liquid Scintillator and LENA as a Far-Detector in an LBNO Experiment 2016.

[20] Mention, G. et al. "Reactor Antineutrino Anomaly." Physical Review D 83.7 (2011): n. pag. Crossref. Web.

[21] M. Tanabashi et al. (Particle Data Group): Physical Review D98, 030001 (2018)

[22] PNGGuru: The Standard Model of Elementary Particles Fundamental interaction, Standard Model of particle physics transparent background PNG clipart, in: www.pngguru.com, URL: https://www.pngguru.com/free-transparent-background-png-clipart-atgta [last visited: 2019-10-17].

[23] Qian, Xin and Peng, Jen-Chieh: Physics with Reactor Neutrinos 2018, also published in: Reports on Progress in Physics, Volume 82, Number 3 (2019).

[24] R. N. Cahn et al., "White Paper: Measuring the Neutrino Mass Hierarchy," prepared forSnowmass 2013, CommunitySummer Study 2013: Snowmass on the Mississippi (Minneapolis, MN, 2013) arXiv:1307.5487 [hep-ex]

[25] Schever, M.: Status of the Jiangmen Underground Neutrino Observatory. Ukrainian Journal of Physics, 64(7), 635 (2019).

[26] Schmitz, Wouter: Particles, Fields and Forces - A Conceptual Guide to Quantum Field - Theory and the Standard Model, Cham (Switzerland): Springer Nature Switzerland AG 2019.

[27] Wonsak, B.S. et al. "Topological Track Reconstruction in Unsegmented, Large-Volume Liquid Scintillator Detectors." Journal of Instrumentation 13.07 (2018): P07005–P07005. Crossref. Web.

[28] Y.Fukuda et al: Evidence for oscillation of atmospheric neutrinos 1998, also published in: Physical Review Letters, Volume 81 (1998).

[29] Zuber, Kai: Neutrino Physics, 2nd ed., Boca Raton (FL,USA): Taylor & Francis Group LLC 2011.

[30] Olive, K. A., Agashe, K., Amsler, C., Antonelli, M., Arguin, J. F., Asner, D. M., ... Schaffner, P. (2014). Review of particle physics. Chinese Physics C, 38(9), [090001]. https://doi.org/10.1088/1674-1137/38/9/090001

[31] Wurm, M. et al. "Optical Scattering Lengths in Large Liquid-Scintillator Neutrino Detectors." Review of Scientific Instruments 81.5 (2010): 053301. Crossref. Web.

[32] Capozzi, F., E. Lisi, and A. Marrone. "PINGU and the Neutrino Mass Hierarchy: Statistical and Systematic Aspects." Physical Review D 91.7 (2015): n. pag. Crossref. Web.

[33] Benckwitz, Felix. "Applications of topological reconstruction to reduce the muon induced background in large volume liquid scintillator ditectors".(2017)

8 Danksagung

Ich möchte mich bei meiner Familie bedanken, die mich während meines Studiums jeder Zeit und auf jede nötige Weise unterstützte. Desweiteren bedanke ich mich hiermit bei all meinen Kommilitonen, die mich immer wieder motivierten und halfen, mein Verständnis für die Physik sowie Mathematik zu verbessern und mit denen ich viele Wochen in der Bibliothek mit rechnen verbrachte. Auch meiner Forschungsgruppe spreche ich einen großen Dank aus, da sie mir bei all meinen Fragen zur Programmierung und Physik ohne zu zögern halfen, wobei einzelne schon einmal viele Stunden ihrer Arbeitszeit für mich in Anspruch genommen haben.

Auch ein Dankeschön an meine Freunde, die ich hier in Hamburg kennen gelernt und mit denen ich eine so schöne Zeit verbringen konnte.

Vielen Dank, ohne Euch hätte es nicht funktioniert!

Eidesstattliche Erklärung

Ich versichere, dass ich die beigefügte schriftliche Bachelorarbeit selbstständig angefertigt und keine anderen als die angegebenen Hilfsmittel benutzt habe. Alle Stellen, die dem Wortlaut oder dem Sinn nach anderen Werken entnommen sind, habe ich in jedem einzelnen Fall unter genauer Angabe der Quelle deutlich als Entlehnung kenntlich gemacht. Dies gilt auch für alle Informationen, die dem Internet oder anderer elektronischer Datensammlungen entnommen wurden. Ich erkläre ferner, dass die von mir angefertigte Bachelorarbeit in gleicher oder ähnlicher Fassung noch nicht Bestandteil einer Studien- oder Prüfungsleistung im Rahmen meines Studiums war. Die von mir eingereichte schriftliche Fassung entspricht jener auf dem elektronischen Speichermedium. Ich bin damit einverstanden, dass die Bachelorarbeit veröffentlicht wird.